MATERIALS SCIENCE

Valence can control the nonexponential viscoelastic relaxation of multivalent reversible gels

Hugo Le Roy[1,2]†*, Jake Song[3,4]†, David Lundberg[5], Aleksandr V. Zhukhovitskiy[6,7], Jeremiah A. Johnson[6], Gareth H. McKinley[8], Niels Holten-Andersen[3,9], Martin Lenz[1,10]*

Gels made of telechelic polymers connected by reversible cross-linkers are a versatile design platform for biocompatible viscoelastic materials. Their linear response to a step strain displays a fast, near-exponential relaxation when using low-valence cross-linkers, while larger supramolecular cross-linkers bring about much slower dynamics involving a wide distribution of timescales whose physical origin is still debated. Here, we propose a model where the relaxation of polymer gels in the dilute regime originates from elementary events in which the bonds connecting two neighboring cross-linkers all disconnect. Larger cross-linkers allow for a greater average number of bonds connecting them but also generate more heterogeneity. We characterize the resulting distribution of relaxation timescales analytically and accurately reproduce stress relaxation measurements on metal-coordinated hydrogels with a variety of cross-linker sizes including ions, metal-organic cages, and nanoparticles. Our approach is simple enough to be extended to any cross-linker size and could thus be harnessed for the rational design of complex viscoelastic materials.

INTRODUCTION

Soft hydrogels are ubiquitous in biology and dictate the mechanics of cells and tissues (*1*). Because of their biocompatibility, synthetic hydrogels are thus prime candidates to serve as robust soft tissue implants, although fine control of their viscoelastic properties is crucial for their success in this role (*2*, *3*). In simple viscoelastic materials, stress relaxes according to a single exponential with a single relaxation time. This is not however the case for most biological materials such as cells (*4*), tissues (*5*), mucus (*6*), and biofilms (*7*). Instead, their relaxation is characterized by a broad distribution of relaxation times (*8*). Such relaxation is often heuristically described by a stretched exponential

$$\sigma(t) \propto e^{-(t/\tau)^{\alpha}} \quad (1)$$

where smaller values of the exponent $\alpha \in]0; 1[$ denote broader distributions of relaxation timescales (*9*). Other similarly phenomenological fitting functions include power-law dependences of σ on t (*10*–*12*) and log-normal distributions of the relaxation times (*13*, *14*).

Associative gels, which relax by a succession of binding and rebinding events (*15*), offer a promising route to design controllable viscoelastic materials. It is thus possible to tune their relaxation time by modifying the dissociation rate (*16*) of their cross-linkers (*17*, *18*). Although this chemistry-based approach allows tuning of the overall stress relaxation time as illustrated in Fig. 1A, less is known about the different approaches to tune the shape of the stress relaxation curve of reversible hydrogels. Accordingly, most existing models for the relaxation of multivalent gels focus on regimes dominated by a single relaxation timescale (*19*), leading to exponential relaxation (*20*). Control over the distribution of relaxation timescales could however be achieved in synthetic hydrogels connected with multivalent dynamic cross-linkers such as nanoparticles (NPs) (*21*), metal-organic cages (*22*), clay (*23*), and latex beads (*24*), which are known to exhibit nonexponential viscoelastic relaxation. Here, we aim to elucidate this emergence of a wide distribution of timescales in materials with high-valence cross-linkers to enable the rational design of complex gels (Fig. 1B). Here, we use the term "valence" to designate the number of polymer strands that a cross-linker can bind, a property sometimes also referred to as their "functionality" (*25*).

We propose that the emergence of a broad distribution of relaxation timescales arises from microscopic events consisting of the severing of the physical connection between two cross-linkers. We first propose a model where this connection, hereafter termed "superbond," breaks if all its constitutive cross-linkers are detached at the same time (Fig. 1B). We show that the breaking time of a superbond increases exponentially with the number of strands involved, consistent with previous observation (*26*). As a result of this strong dependence, small spatial heterogeneities in the polymer concentration may result in widely different relaxation times from one superbond to the next. Such exponential amplification of relaxation times originating from small structural differences forms the basis of models previously used to describe the relaxation of soft glasses (*27*–*29*). In contrast with these studies, our approach explicitly models the microscopic basis of this amplification. That allows it to not only recover relaxation curves virtually indistinguishable from those discussed in previous studies but to also predict the influence of temperature and cross-linker valence on the macroscopic stress relaxation observed in the resulting gel. The details of the polymer strand morphology are not central to this influence, and we thus enclose them in a few effective parameters that could be derived from first principles in specialized models related to specific implementations of our basic mechanism. To confirm these predictions,

[1]Université Paris-Saclay, CNRS, LPTMS, 91405, Orsay, France. [2]Institute of Physics, École Polytechnique Fédérale de Lausanne (EPFL), 1015 Lausanne, Switzerland. [3]Department of Materials Science and Engineering, Massachusetts Institute of Technology, 77 Massachusetts Avenue, Cambridge, MA 02139, USA. [4]Department of Mechanical Engineering, Stanford University, Stanford, CA 94305, USA. [5]Department of Chemical Engineering, Massachusetts Institute of Technology, 77 Massachusetts Avenue, Cambridge, MA 02139, USA. [6]Department of Chemistry, Massachusetts Institute of Technology, 77 Massachusetts Avenue, Cambridge, MA 02139, USA. [7]Department of Chemistry, University of North Carolina at Chapel Hill, Chapel Hill, NC 27599, USA. [8]Department of Mechanical Engineering, Massachusetts Institute of Technology, 77 Massachusetts Avenue, Cambridge, MA 02139, USA. [9]Department of Bioengineering and Materials Science and Engineering, Lehigh University, Bethlehem, PA 18015, USA. [10]PMMH, CNRS, ESPCI Paris, PSL University, Sorbonne Université, Université de Paris, F-75005 Paris, France.
*Corresponding author. Email: h.leroy@epfl.ch (H.L.R.); martin.lenz@universite-paris-saclay.fr (M.L.)
†These authors contributed equally to this work.

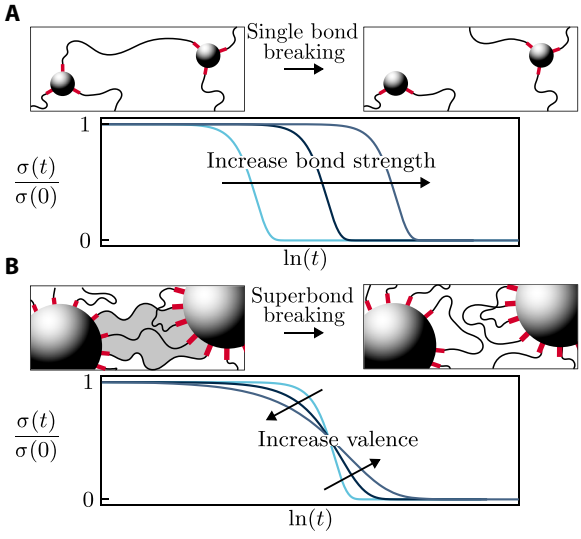

Fig. 1. High-valence cross-linkers yield a slow, potentially complex unbinding dynamics. (**A**) Hydrogels held together by small cross-linkers relax over the timescale associated with the unbinding of a single polymer strand. There, stress decays exponentially in response to a step strain: $\sigma(t)/\sigma(0) = \exp(-t/\tau)$. Since $t/\tau = \exp(\ln t - \ln \tau)$, changes in the timescale τ shift the σ versus $ln\ t$ relaxation curve horizontally but do not alter its shape. (**B**) In contrast, relaxation events in the presence of high-valence cross-linkers require the simultaneous unbinding of many polymer stands. The associated timescale is long and highly variable depending on the number of strands involved in the superbond (gray shade). As a result, the stress relaxation of such gels is no longer exponential, and the precise shape of the relaxation curve strongly depends on the valence of the cross-linkers. In practical cases, changes in valence are typically accompanied by an additional shift of the curves toward larger relaxation times not shown in this illustrative schematic.

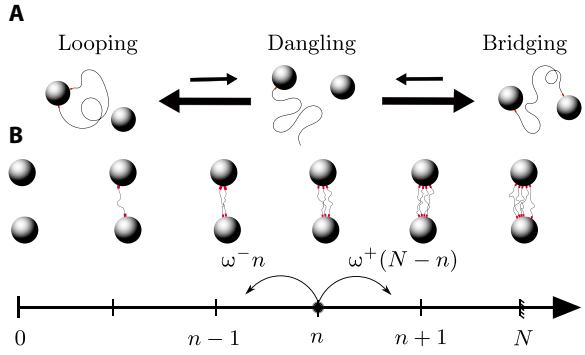

Fig. 2. We model superbond breaking as the disconnection of many independent polymer strands. (**A**) Disconnecting a single polymer strand requires going through a high-energy, short-lived dangling state (larger arrows indicate faster transitions). The looping and bridging states both have two polymer–cross-linker bonds and therefore have the same energy. (**B**) Individual strands in a superbond attach and detach independently, resulting in a one-dimensional random walk in the number n of attached strands (Eq. 3). Here, we only draw the bridging strands and not the looping strands.

we conduct experiments on hydrogels with four distinct cross-linker types of different sizes and find that our model quantitatively reproduces multiple relaxation curves using this small set of microscopic parameters. Last, we show that several phenomenological fitting functions used in the literature can be recovered as asymptotic regimes of our analytical model.

RESULTS

Model of a single superbond

We first model a single superbond in the simple, experimentally relevant (*22*) case of strong interactions combined with short polymers, which implies negligible entanglements as discussed in Methods. In the limit of very large and rigid cross-linkers, the polymer layer around a cross-linker is locally planar, its structure is not affected by small fluctuations of polymer concentration, and its thickness fixes the distance between cross-linkers (*22*, *30*). We thus use the simplifying assumption that all individual bonds participating in a superbond are identical and noninteracting, an approximation whose validity we ultimately assess through comparisons with experiments.

We model the attachment and detachment of a single polymer strand from a pair of cross-linkers as shown in Fig. 2A. When both its ends are bound, the strand may or may not connect two different cross-linkers. The corresponding "bridging" and "looping" states have the same energy since we assume the polymer strand to be completely flexible, and we denote by ΔS the entropy difference between them. To transition between these two states, the strand must disconnect one of its ends and form a "dangling" state. The disconnection of the strand in this state implies an energy barrier ΔE that is much larger than the thermal energy $k_B T = \beta^{-1}$. This implies that the dangling state is short-lived, and thus need not be explicitly included in our modeling. Our approximation scheme implies that the overall rate ω^+ and ω^- to go from the looping to the bridging state and back are constant. They read

$$\omega^+ = \frac{1}{\tau_0} e^{-\beta \Delta E} \qquad \omega^- = \frac{1}{\tau_0} e^{-\beta \Delta E + \Delta S} \tag{2}$$

where the typical timescale τ_0 takes into account the entropy difference between the looping and dangling state. At equilibrium, we denote the probability for a single polymer strand to create a bridge as $p_{on} = 1 - p_{off} = 1/(1 + e^{\Delta S})$.

We now consider the dynamic of a single superbond. In the limit of small polymer strands and large cross-links, we neglect the exchange of polymer strands between superbonds. Each superbond thus fluctuates independently of the other superbonds belonging to the same cross-linker. In that case, the total number of polymer strands in a superbond is fixed in time, and we denote it by N. Within our approximation of independent attachment and detachment of the individual polymer strands, the superbond undergoes the Markov process illustrated in Fig. 2B and the probability $P_n(t)$ for n strands to create bridges between the two cross-linkers at time t satisfies the master equation

$$\partial_t P_n(t) = (N-n+1)\,\omega^+ P_{n-1}(t) + (n+1)\,\omega^- P_{n+1}(t) - [(N-n)\,\omega^+ + n\,\omega^-] P_n(t) \tag{3}$$

which can be derived as the master equation whereby a state with n bridging and $(N - n)$ looping strands gains one with transition rate $(N - n)\omega^+$ and loses one with $n\omega^-$ (*31*). Equation 3 ensures that the number of bridging strands n is always comprised between 0 and N, which must be the case as each strand in our model has exactly two bonds and is thus either bridging or looping (Fig. 2).

To determine the rate at which a superbond breaks, we set an absorbing boundary condition $P_0(t) = 0$ and define its survival probability as $S(t) = \sum_{n=1}^{N} P_n(t)$. In the limit $N \gg 1$ where a large number of strands are involved in the superbond, we show in section S1 that the detachment of the two beads is analogous to a Kramers escape problem. We thus prove that the survival probability decays as a single exponential $S(t) = \exp(-t/\tau_N)$ (*32*) with an average detachment time

$$\tau_N \underset{N\to\infty}{\sim} \frac{\tau_0 e^{\beta\Delta E}}{N p_{off}^N} \quad (4)$$

The breaking of the superbond can thus be assimilated to a Poisson process with rate $1/\tau_N$ regardless of the initial condition $P_n(0)$. The strong, exponential dependence of τ_N on N implies that any dispersity in the number of strands involved in a superbond may result in a wide distribution of timescales.

Model of the relaxation of a gel

Two factors influence the dispersity of *N*. First, its value is constrained by the available space at the surface of each cross-linker, which we model by setting an upper bound N_{sat} on the number of polymer strands (in a loop or a bridge) participating in any superbond. Second, depending on the local density of polymer in the vicinity of the superbond, the actual number of strands present may be lower than N_{sat}. In the regime where the polymer solution surrounding the cross-linkers is dilute, polymer strands are independently distributed throughout the system. As a result, the distribution of local strand concentrations within a small volume surrounding a superbond follows a Poisson distribution. We thus assume that *N* is also described by a Poisson distribution up to its saturation at N_{sat}

$$p(N) = \begin{cases} \dfrac{\overline{N}^K e^{-\overline{N}}}{N!} & \text{for } N < N_{sat} \\ \displaystyle\sum_{K=N_{sat}}^{+\infty} \dfrac{\overline{N}^K e^{-\overline{N}}}{N!} & \text{for } N = N_{sat} \end{cases} \quad (5)$$

where $\overline{N}$ would be the average number of strands in a superbond in the absence of saturation and thus depends on the ratio of polymer to cross-linker concentration. Note that the specific form of the distribution used in Eq. 5 does not substantially modify our results, as discussed later.

In response to a step strain, we assume that each superbond is stretched by an equal amount and resists the deformation with an equal force before breaking. Superbonds may subsequently reform, but the newly formed bonds are not preferentially stretched in the direction of the step strain and therefore do not contribute to the macroscopic stress on average. Denoting by $t = 0$ the time at which the step strain is applied and by $\sigma(t)$ the resulting time-dependent shear stress, the progressive breaking of the initial superbonds results in the following stress response function

$$\frac{\sigma(t)}{\sigma(t=0)} = \sum_{N=1}^{N_{sat}} \frac{p(N)}{1-p(0)} e^{-t/\tau_N} \quad (6)$$

While the breaking times τ_N are unaffected by the applied stress in the linear response regime, nonlinearities could easily be included in our formalism by making ΔS stress-dependent and thus favoring strand detachment. The relaxation described in Eq. 6 occurs in two stages. At long times $t \gg \tau_{N_{sat}}$, few short-lived superbonds remain. Saturated superbonds ($N = N_{sat}$) dominate the response, and Eq. 6 is dominated by the last term of its sum. As a result, the stress relaxes exponentially over time, as seen from the linearity of the log-lin curves of Fig. 3A for large values of *t*. Systems with smaller values of N_{sat} manifest this regime at earlier times; in the most extreme case, where superbonds involve at most a single polymer strand ($N_{sat} = 1$), the relaxation of the system is fully exponential and extremely fast as compared to systems with higher N_{sat}. Over short times ($t \ll \tau_{N_{sat}}$), stress relaxation involves multiple timescales. This nonexponential regime is apparent on the left of Fig. 3A. These two regimes have already been reported in several experimental gels connected by multivalent dynamic cross-linkers (*1*, *30*).

While Eq. 6 is not identical to the stretched exponential of Eq. 1, the inset of Fig. 3B shows that they are remarkably close in practice. We thus relate the stretch exponent α to the saturation number N_{sat} by fitting a stretched exponential to our predicted stress response function over the time interval required to relax 90% of the initial stress (Fig. 3B). The fits are very close matches and consistently give correlation factors $r^2 > 0.98$ (see detailed plots in fig. S2). If $N_{sat} \lesssim 0.5\overline{N}$ then $\alpha \simeq 1$, indicating a nearly exponential relaxation. In that case, superbond saturation occurs well before the peak of the Poisson distribution of *N*. Physically, this implies that the local polymer concentration surrounding most superbonds is sufficient to saturate them. As almost all superbonds are saturated, they decay over the same timescale $\tau_{N_{sat}}$. As a result, the material as a whole displays an exponential relaxation. For larger values of N_{sat}, the Poisson distribution is less affected by the saturation, and the dynamics is set by the successive decay of superbonds involving an increasing number of strands, implying lower values of α. The larger the value of $\overline{N}$, the sharper the crossover between these two regimes.

Experiments

To validate our model of the effect of cross-linker valence on hydrogel relaxation, we perform step-strain experiments of poly(ethylene glycol) (PEG)–based gels involving a range of cross-link valences and compare Eq. 6 to the resulting relaxation curves. We implement

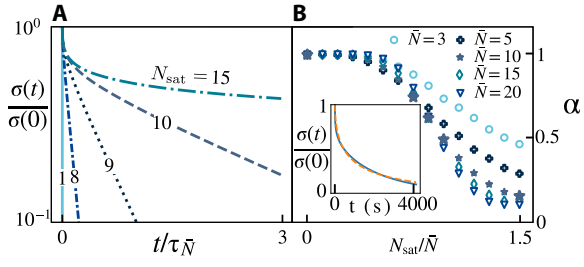

Fig. 3. Influence of the valency on the stretch exponent. (**A**) Disperse, high-valence superbonds initially display a nonexponential mechanical relaxation and then cross over to an exponential regime when only the saturated superbonds remain. Curves plotted from Eq. 6 with $p_{off} = 0.2$, $\overline{N} = 10$ and different values of N_{sat} as indicated on each curve. (**B**) Relationship between the stretch exponent α quantifying the nonexponential character of the relaxation and the microscopic parameter $N_{sat}/\overline{N}$. Here $p_{off} = 0.2$. A low $N_{sat}/\overline{N}$ gives an exponential relaxation ($\alpha \simeq 1$), while a larger $N_{sat}/\overline{N}$ leads to a more complex behavior ($\alpha < 1$). While α appears to converge to a finite value for large $N_{sat}/\overline{N}$ for the largest values of $\overline{N}$, this behavior is contingent on our choice of fitting interval. This issue does not affect the rest of the curves. Large stars correspond to the curves represented in (A). Inset, illustration of the quality of the fits between the heuristic stretched exponential (dashed orange line, Eq. 1) and our prediction (solid blue line, Eq. 6).

two sets of metal-cooordination chemistry: nitrocatechol-Fe^{3+} coordination and bispyridine-Pd^{2+} coordination. The first set of gels is made with nitrocatechol-functionalized PEG cross-linked by single Fe^{3+} ions with an estimated valence of 3, and by iron oxide NPs. The NPs have a mean diameter of 7 nm with a surface area that allows a valence of ~100 ligands (*21*). The second set of gels are made with bispyridine-functionalized PEG, wherein bis-*meta*-pyridine ligands induce self-assembly of gels that are cross-linked by Pd_2L_4 nanocages with a valence of 4, and bis-*para*-pyridine ligands induce self-assembly of gels that are cross-linked by $Pd_{12}L_{24}$ nanocages with a valence of 24 (*33*). As shown in Fig. 3, these four distinct gel designs result in a broad range of relaxation behaviors. Overall, large-valence gels and lower temperatures result in longer relaxation times, consistent with the illustration of Fig. 1A. The relaxation curves associated to high-valence cross-linkers are also less steep, consistent with the involvement of a broader distributions of relaxation times and the schematic of Fig. 1B.

To demonstrate the application of the model based on these valency values, we estimate the value of N_{sat} associated with each system based on an initial hypothesis that each cross-linker is connected to six nearest neighbors, i.e., N_{sat} = valence/6 (rounded to an integer in Table 1). This represents an upper bound estimate (*34*, *35*) of the number of nearest neighbors in the gel; the actual number could be estimated through molecular simulations (*36*).

At a more detailed level, our assumption that the dynamics of single polymer strand proceeds independently of its environment implies the existence of a single energy scale ΔE. As a result, we predict that all timescales involved in the relaxation are proportional to $\exp(-\beta\Delta E)$. We confirm this through a time-temperature collapse shown in the insets of Fig. 3 (see section S4 for details). This collapse provides us with the value of ΔE for each of our four systems, which we report in Table 1. The binding energy value ΔE for the Pd_2L_4 and $Pd_{12}L_{24}$ gels match, as expected from the fact that they originate from the same composition. On the other hand, the ΔE of the NP gels appear to be lower than the Fe^{3+} ion gels, which is due to the reduced electron availability of the Fe sites on the NP surface. Moreover, the environment used to make NP gels is more acidic than the ion gels, which modifies the ligand affinity.

To compare the temperature-collapsed curves to our prediction of Eq. 6, we fit the parameters p_{off}, τ_0, $\overline{N}$, and N_{sat} across multiple temperatures. The resulting fits, shown in Fig. 4, display a good agreement between the theory and experiments across up to four

Table 1. Estimated and fitted parameters involved in the comparison between experiment and theory in Fig. 4. The energies are given in units of k_BT for $T = 300$ K. Instead of displaying the parameter τ_0, we present the more easily interpreted unbinding time of a single polymer strand at 300 K, namely $\tau_1 = \tau_0 e^{\beta 300 \Delta E} / p_{off}$.

Cross-linker	Fe^{3+}	Pd_2L_4	$Pd_{12}L_{24}$	Nanoparticles
Estimated valence	3	4	24	100
N_{sat}	1	4	7	17
ΔE (units of k_BT)	28	24	24	24
p_{off}	0.08	0.15	0.15	0.36
τ_1 at $T = 300$ K (s)	1.7	6.1	1.9	0.1
$\overline{N}$	1w	6	9	14

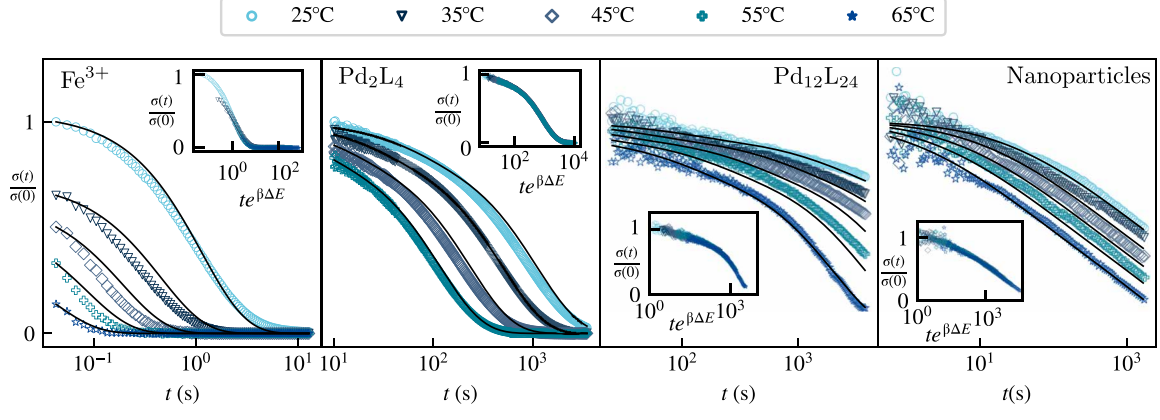

Fig. 4. Stress relaxation function for four experimental systems with increasing cross-linker valences (see Table 1 for values). The averaged correlation coefficients for the fits of each panel from left to right are: 0.98, 0.99, 0.94, and 0.96. Here, we use a log-lin scale (unlike in Fig. 3A) to facilitate the visualization a large range of timescales. Alternate representations are available as fig. S5. Symbols are experimental data points, and the lines are the associated fitting curves. Insets, time-temperature collapsed data obtained by a rescaling $t \rightarrow te^{\beta\Delta E}$.

orders of magnitude in timescales. The fitted values of N_{sat} consistently increase with the estimated valence of the cross-linkers (Table 1), a trend that confirms our interpretation of the physical origin of N_{sat}. The specific numerical values of these two quantities do not however match exactly, pointing to a possible gap in our understanding of the structure of each category of gels, and, in particular, the number of nearest neighbors of an individual cross-link, which remains debated for these types of gels (*34*–*36*). The possible clustering of cross-linkers may also influence this relation, as nanocage systems similar to ours (*37*) may form higher-order nanocage structures. While such complexities as well as possible imperfections in our fitting procedure complicate the literal interpretation of the fitted values of N_{sat}, the global trend confirms our interpretation of its physical origin. The fit also supports the notion that the mean number of strands per superbond $\overline{N}$ accounts for the distribution of relaxation timescales in our gels. The Fe^{3+} gel thus displays an exponential relaxation consistent with $\overline{N} = N_{sat} = 1$. The higher-valence Pd_2L_4 and $Pd_{12}L_{24}$ systems have a complex relaxation at early times followed by an exponential behavior, as expected for $\overline{N} \simeq N_{sat} > 1$. As expected from our model, the crossover time $\tau_{N_{sat}}$ separating the two regimes is larger in the higher-valence $Pd_{12}L_{24}$ gel. Finally, the high-valence NP system shows an extended complex relaxation associated with $\overline{N} < N_{sat}$, thus confirming that all the qualitative relaxation regimes discussed in the previous sections are experimentally relevant.

Distribution of relaxation timescales

To further visualize the differences between the responses of our gels, we plot the distributions of relaxation times $p(\tau)$ for our fitted model in Fig. 5. The Fe^{3+} gels, which relax according to a single exponential and whose $p(\tau)$ are therefore delta functions, are not represented there. In the Pd_2L_4 and $Pd_{12}L_{24}$ systems, a distribution characterized by an initially decreasing distribution of timescales is interrupted by a valence-dependent maximum relaxation time $\tau_{N_{sat}}$. That time is comprised within the range of timescales observed in Fig. 4, accounting for the crossover to an exponential relaxation within this range. In NP systems, by contrast, the crossover occurs much later and thus cannot be directly observed in experiments. In all cases, the precise form of the distribution of timescales used in the domain $\tau < \tau_{N_{sat}}$ does not critically affect the predicted relaxation curves. We show in section S6 that replacing the Poisson distribution of Eq. 5 with other distributions with the same mean and variance lead to essentially indistinguishable predictions over experimentally observable timescales. This emphasizes the robustness of our predictions to the details of that choice of distribution. They are instead primarily determined by the mean and maximum superbond sizes, $\overline{N}$ and N_{sat}.

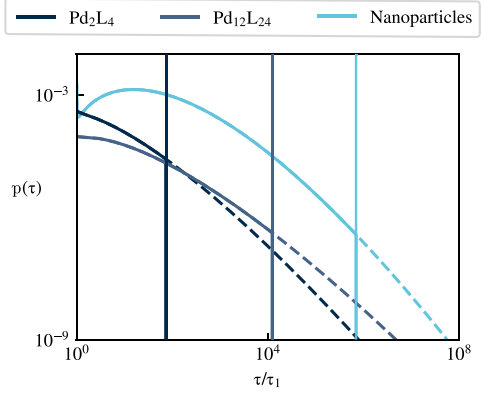

Fig. 5. Distribution of relaxation times corresponding to the theoretical plots of Fig. 4. The distribution associated with the Fe^{3+} gel is a delta function for $\tau/\tau_1 = 1$ and is thus not represented on this graph. The time distributions are given by a Poisson distribution cut for $\tau = \tau_{N_{sat}}$ (vertical lines), as described in Eq. 6. The dotted lines represent what these distributions would be in the absence of this saturation.

In the limit of large $\overline{N}$ and even larger N_{sat}, the complex relaxation phase of our model characterized by $t < \tau_{N_{sat}}$ may display analytical behaviors identical to some widely used rheological fitting functions. In this regime, the Poisson distribution $p(N)$ of Eq. 5 goes to a Gaussian. Since, according to Eq. 4, the variable N is essentially the logarithm of the relaxation time τ for $\overline{N} \gg 1$, this results in a log-normal distribution of relaxation timescales

$$p(\tau) = \frac{1}{\sqrt{2\pi\overline{N}}\,|\ln p_{off}|\,\tau} \times \exp\left\{ -\frac{\left[\ln\tau + \ln\frac{\overline{N}}{\tau_1} + \ln p_{off}(\overline{N}-1)\right]^2}{2\overline{N}(\ln p_{off})^2} \right\} \tag{7}$$

This result adds additional insights to this widely used fitting functional form, as it allows us to relate the mean and variance of the distribution to the underlying cross-linker–scale parameters (*13*, *14*). It moreover offers a potential molecular-level justification for its use in describing the complex relaxation of systems with multivalent cross-links. In the alternative case where $p(N)$ is a decaying exponential, our model results in power-law distributed relaxation timescales, and the stress response function takes the form

$$\sigma(t) \propto t^{-\gamma}, \text{ with } \gamma = \frac{1}{\overline{N}\,|\ln p_{off}|} \tag{8}$$

This result may also be presented in terms of the dependence of the storage and loss moduli on the frequency ω in an oscillatory rheology experiment. We thus predict that for $\gamma < 1$

$$G'(\omega) \approx \begin{cases} \omega^2 & \text{for } \omega \ll \tau_{N_{sat}}^{-1} \\ \omega^{\gamma} & \text{for } \tau_{N_{sat}}^{-1} \ll \omega \ll \tau_1^{-1} \\ \omega^0 & \text{for } \tau_1^{-1} \ll \omega \end{cases} \tag{9a}$$

$$G''(\omega) \approx \begin{cases} \omega^1 & \text{for } \omega \ll \tau_{N_{sat}}^{-1} \\ \omega^{\gamma} & \text{for } \tau_{N_{sat}}^{-1} \ll \omega \ll \tau_1^{-1} \\ \omega^{-1} & \text{for } \tau_1^{-1} \ll \omega \end{cases} \tag{9b}$$

The results for larger values of γ and detailed derivations of Eqs. 7 to 9 are shown in the Supplementary Materials. Again, this result has the potential to account for the power-law relaxation observed in many rheological systems (*10*–*12*), in addition to providing a link to their microscopic constituents. Overall, these results suggest a possible control of the system's rheology through the characteristics of $p(N)$, which could in turn be modulated through the spatial distribution of the polymer strands and the dispersity of the cross-linkers.

DISCUSSION

Our simple model recapitulates a wide range of rheological behaviors in multivalent systems based on two key superbond parameters: the mean size $\overline{N}$ and the maximum size N_{sat}. These respectively control the amplitude of the fluctuations in superbond size and the longest superbond relaxation timescale. Before the longest relaxation time, the system displays an increasingly nonexponential response for increasing $\overline{N}$ (Fig. 3B). Beyond it, it crosses over into exponential relaxation. In contrast with widely used phenomenological fitting parameters, our two variables yield reliable insights into the underlying microscopic dynamics, as demonstrated by the agreement of their fitting values with our a priori knowledge of four experimental systems covering a wide range of values of $\overline{N}$ and N_{sat}.

Our model bears a mathematical similarity with standard random energy trap models (*38*). There, a long-tailed relaxation emerges from a short-tailed distribution of trap depths due to the exponential dependence of the relaxation times on the trap depths. Similarly, here, a nonexponential relaxation emerges from a short-tailed distribution of superbond sizes N (Eq. 5) thanks to the exponential dependence of τ_N on N (Eq. 4). In contrast with trap models, however, our model does not predict a glass transition upon a lowering of temperature. It instead displays a simple Arrhenius time-temperature relation, consistent with the experimental collapses in the insets of Fig. 4. Another related relaxation process is manifested in multivalent polymer chains, which interact through multiple sticky domains. Recent data involving relatively short such chains suggest a relaxation mode governed by the simultaneous detachment of all stickers carried by a polymer, implying an exponential dependence of the relaxation time on valence similar to ours (*39*). The resulting macroscopic relaxation dynamics is however essentially exponential, either because of the relatively small valences involved or because valence fluctuations affect flexible polymers differently than our rigid cross-linkers. Such systems also display more complicated relaxation modes, from sticky Rouse-like diffusion to localized collective motions due to nanodomain clustering (*40*). The reasonable agreement between our estimated valences and the fitted values of N_{sat} suggests that while related, the relaxation mechanisms in our rigid cross-linker systems may be easier to relate to simple geometrical characteristics of their components.

Our model's focus on the collective aspects of superbond breaking and the characteristics of the cross-linkers implies that it encloses most of the physics of the polymer strands within a few mesoscopic parameters, mainly τ_0 and ΔS. Within our approach, the morphology of the polymer thus does not affect the form of our relaxation, although it may lead to a rescaling of the relaxation times of Eq. 4. This formulation remains valid as long as the length and concentration of the polymer strands is low enough that the strands do not become significantly entangled, which could spoil the Poissonian attachment/detachment process of Eq. 2. Even in this case, however, this equation may not be strictly valid, as the polymer layer in a superbond with many bound cross-linkers tends to be more compressed than in one with few. This effect should lead to a smooth (likely power law) dependence of $\omega^{\pm}$ on N, which would preserve the dominance of the much more abrupt exponential dependence of τ_N on N. As a result, while such polymer brush effects could induce corrections in our estimations of the model parameters, the basic mechanism outlined here should still hold in their presence. The overall cross-linker and strand concentrations mainly influence two other model parameters, namely N_{sat}, which depends on the number of neighbors of each cross-linker, and $\overline{N}$, which counts the average number of available strands per superbond. Another assumption of our model is that neighboring superbonds do not exchange polymer strands. This is correct in our limit of short, strongly bound strands, which are unlikely to reach out to the next superbond or migrate toward it. While our experimental systems are not a priori guaranteed to be far into this asymptotic regime, the good agreement with our predictions suggests that it constitutes a reasonable approximation. Overall, it is worth keeping in mind that while many aspects of our model are idealized, its key result, namely the exponential dependence of τ_N on N, is very robust to the introduction of more realistic, system-dependent features in the model. Such features thus leave our central conclusions about the influence of valence on the hierarchy of relaxation timescales intact, although they might modify our interpretation of certain model parameters. For instance, a possible clustering interaction between ligands on the surface of the cross-linker would imply that the energy ΔE is actually a sum of a ligand–cross-linker and a ligand-ligand interaction.

Our model reproduces several qualitative characteristics of the rheology of multivalent gels, such as the strong influence of the cross-linker valence, Arrhenius temperature dependence, and the transition between a nonexponential and an exponential regime at long times. Because of its simple, widely applicable microscopic assumptions, we believe that it could help shed light on and assist the design of a wide range of multivalent systems. Beyond composite gels, it could thus apply to RNA-protein biocondensates where multivalent interactions between proteins are mediated by RNA strands (*41*), as well as cytoskeletal systems where filaments linked to many other filaments display a slow relaxation reminiscent of that of our multivalent cross-linkers (*42*).

METHODS

Estimate of the amount of entanglements in our NP system

Our 10-kDa stars comprise 28 Kuhn segments per arm, each with length 0.76 nm (*43*), implying a radius $R \simeq 4$ nm. As the overall polymer density in our system is $c = 10^{-4}$ mol ml^{-1}, this implies that the concentration of our solution is lower than the overlap concentration

$$\frac{c}{c^*} = c\frac{4\pi R^3}{3} \simeq 0.64 \tag{10}$$

and therefore that our initial solution is not entangled.

Now considering the situation within a single superbond between two 7-nm NP as opposed to the average situation within the solution, the polymer size and the fitted values of Table 1 suggest that a superbond contains the equivalent of $\overline{N} = 14$ bifunctional polymer strands in a volume of the order of that of a particle. This yields a packing length (typical distance between entanglements) $p \simeq 2$ nm (*44*). This suggests that each chain is entangled once or a few times with its neighbors, which could slow down the system's relaxation dynamics, but which we do not expect to impose topological constraints strong enough that the polymer's reptation time would differ from its Rouse time by orders of magnitude.

Materials

4-arm PEG bis(acetic acid *N*-succinimidyl) ester (4-arm PEG-NHS) (M_W = 10 kDa) and 1-arm PEG-NHS (M_W = 2000 Da) were

purchased from JenKem Technology. Sodium sulfate (Na_2So_4), sodium nitrite ($NaNO_2$), iron(III) acetylacetonate [$(Fe(acac)_3$], hydrochloric acid (HCl), dopamine hydrochloride, triethylamine (TEA), *N*-methylmorpholine (NMM), dimethyl sulfoxide (DMSO), methanol (MeOH), ethanol (EtOH), dichloromethane (DCM), *N*,*N*′-dimethylformamide (DMF), diethyl ether (Et_2O), and chloroform ($CHCl_3$), were purchased from Sigma-Aldrich. All chemicals were used without further purification.

Synthesis of 1-arm PEG-catechol

Two hundred and twenty eight milligrams of dopamine hydrochloride is neutralized for 15 min with 0.3 ml NMM in 7.5 ml of dry DMF under N_2 atmosphere. Then, 1 g of mPEG-NHS ($M_W = 2000$ Da) dissolved in 7.5 ml of DMF is added, and the mixture is stirred with N_2 protection at room temperature for 24 hours. The reacted solution is acidified by adding 15 ml of 1 M HCl (aq), and the product is extracted with $CHCl_3$ three times. The organic layers are pooled together and dried with $NaSO_4$, and solvent is removed by rotary evaporation. Last, the product concentrate is precipitated in cold Et_2O (−20°C), filtered, and dried. 1H nuclear magnetic resonance (NMR) (300 MHz, D_2O) δ parts per million (ppm): 6.7 to 6.8 (m, 3H, aromatic), 3.3 to 4.0 (m, $-O-CH_2-CH_2-$), 3.4 (t, 2H, CH_2 adjacent to aromatic ring), 2.7 (t, 2H, $-CH_2-NH-CO-$).

Synthesis of 4-arm PEG-nitrocatechol

One hundred and seventy-eight milligrams of nitrodopamine hydrogen sulfate is neutralized for 15 min with 110 μl of NMM in 4 ml of dry DMF under N_2 atmosphere. Then, 1 g of 4-arm PEG-NHS (M_W = 10 kDa) dissolved in 4 ml of DMF is added, and the mixture is stirred with N_2 protection at room temperature for 24 hours. The reacted mixture is mixed with 15 ml of 1 M $HCl_{(aq)}$, dialyzed with water (MWCO = 3500 Da) for 2 days (water exchanged for more than five times), and freeze-dried. 1H NMR (300 MHz, D_2O) δ (ppm): 7.6 (m, 1H, aromatic), 6.7 (m, 1H, aromatic), 3.6 to 3.9 (m, $-O-CH_2-CH_2-$), 3.5 (t, 2H, CH_2 adjacent to aromatic ring), 3.1 (t, 2H, $-CH_2-NH-CO-$).

Synthesis of Fe_3O_4 NPs

Bare Fe_3O_4 NPs are synthesized following previously reported methods (*44*). One hundred milligrams as-synthesized NPs are redispersed in 80 ml of 1:1 (v/v) solution of $CHCl_3$ and DMF, and 100 mg 1-arm PEG-C is added. The mixture is homogenized and equilibrated by pulsed sonication (pulse: 10 s on +4 s off; power: 125 W) for 1 hour. Then, the mixture is centrifuged at 10,000 rpm for 10 min to remove any aggregates and rotary evaporated at 50°C, 30 mbar to remove $CHCl_3$. Then, the NP solution is precipitated in 150 ml cold Et_2O (−20°C). The precipitate is redispersed in H_2O and freeze-dried. The resulting NPs are 7 nm in diameter.

Preparation of the $Fe3^+$-NC gels

Preparation procedure is similar to a previously reported protocol (*45*), except that the gel is made in DMSO instead of H_2O. Fifty microliters of 4-arm PEG-NC solution (200 mg/ml) in DMSO is mixed with 16.7 μl of 80 mM $FeCl_3$ solution in DMSO (ligand: Fe^{3+} molar ratio of 3:1). Then, 33.3 μl of DMSO and 13.8 μl of TEA is added to facilitate deprotonation, and a gel is formed.

Preparation of the Pd_2L_4 gels

The synthesis of polymer and gel preparation procedures for P_2L_4 is the same as a reported protocol (*33*) with minor modifications. The annealing of the Pd_2L_4 polyMOC gel was done at 60 Â°C for 1 hours instead of 80°C for 4 hours and 1.05 equivalent of $Pd(NO_3)_2$. 2 H_2O (relative to bifunctional polymer ligand) was used instead of 1 equivalent.

Preparation of the $Pd_{12}L_{24}$ gels

The synthesis of polymer and gel preparation procedures for polyMOC is the same as a reported protocol (*33*).

Preparation of the NP gels

Preparation procedure is the same as the reported protocol (*46*). Briefly, PEGylated Fe_3O_4 NPs (equivalent to 20-mg Fe_3O_4 core) and 20-mg 4-arm PEG-NC are mixed in a 0.2 M HCl aqueous solution. The solution mixture (pH 2) is transferred into a mold and sealed, and a solid gel is obtained after curing in a 50°C oven for 24 hours.

Rheology

Stress relaxation measurements are done on an Anton Paar rheometer with parallel plate geometry (10-mm diameter flat probe for NP gels and polyMOC gels and 25-mm diameter cone probe for Fe^{3+} gels). All tests are done immediately after transferring the gel sample onto the sample stage. A Peltier hood is used for all experiments to control the measurement temperature and prevent solvent evaporation. H_2O-based samples are furthermore sealed with mineral oil before experimentation to reduce the evaporation rate. Relaxation tests were performed by applying a $\gamma = 0.005$ step strain for the NP gel and $\gamma = 0.02$ step strain for the other three systems.

Supplementary Materials

This PDF file includes:

Figs. S1 to S8
Table S1
Sections S1 to S9

REFERENCES AND NOTES

1. O. Ronsin, C. Caroli, T. Baumberger, Glass-like dynamics of the strain-induced coil/helix transition on a permanent polymer network. *J. Chem. Phys.* **144**, 064904 (2016).
2. A. C. Borges, C. Eyholzer, F. Duc, P.-E. Bourban, P. Tingaut, T. Zimmermann, D. P. Pioletti, J.-A. E. Månson, Nanofibrillated cellulose composite hydrogel for the replacement of the nucleus pulposus. *Acta Biomater.* **7**, 3412–3421 (2011).
3. O. Chaudhuri, L. Gu, M. Darnell, D. Klumpers, S. A. Bencherif, J. C. Weaver, N. Huebsch, D. J. Mooney, Substrate stress relaxation regulates cell spreading. *Nat. Commun.* **6**, 6365 (2015).
4. P. Kollmannsberger, B. Fabry, Linear and non-linear rheology of living cells. *Annu. Rev. Mat. Res.* **41**, 75–97 (2011).
5. O. Chaudhuri, J. Cooper-White, P. A. Janmey, D. J. Mooney, V. B. Shenoy, Effects of extracellular matrix viscoelasticity on cellular behaviour. *Nature* **584**, 535–546 (2020).
6. J. P. Celli, B. S. Turner, N. H. Afdhal, S. Keates, I. Ghiran, C. P. Kelly, R. H. Ewoldt, G. H. McKinley, P. So, S. Erramilli, R. Bansil, Helicobacter pylori moves through mucus by reducing mucin viscoelasticity. *Proc. Natl. Acad. Sci. U.S.A.* **106**, 14321–14326 (2009).
7. S. Fabbri, P. Stoodley, Mechanical properties of biofilms. *The Perfect Slime—Microbial Extracellular Polymeric Substances* (2016), pp. 153–178.
8. J. Song, N. Holten-Andersen, G. H. McKinley, Non-Maxwellian viscoelastic stress relaxations in soft matter. *Soft Matter* **19**, 7885–7906 (2023).
9. J. -P. Bouchaud, Anomalous relaxation in complex systems: From stretched to compressed exponentials, in *Anomalous Transport* (John Wiley & Sons Ltd, 2008), chap. 11, pp. 327–345.
10. G. W. Scott Blair, J. Burnett, On the creep, recovery, relaxation and elastic "Memory" of some renneted milk gels. *Br. J. Appl. Phys.* **10**, 15–20 (1959).
11. B. Keshavarz, T. Divoux, S. Manneville, G. H. McKinley, Nonlinear viscoelasticity and generalized failure criterion for polymer gels. *ACS Macro Lett.* **6**, 663–667 (2017).
12. M. Balland, N. Desprat, D. Icard, S. Féréol, A. Asnacios, J. Browaeys, S. Hénon, F. Gallet, Power laws in microrheology experiments on living cells: Comparative analysis and modeling. *Phys. Rev. E* **74**, 021911 (2006).

13. E. S. Epstein, L. Martinetti, R. H. Kollarigowda, O. Carey-de la Torre, J. S. Moore, R. H. Ewoldt, P. V. Braun, Modulating non-covalent cross-links with molecular switches. *J. Am. Chem. Soc.* **141**, 3597–3604 (2019).
14. R. J. Masurel, S. Cantournet, A. Dequidt, D. R. Long, H. Montes, F. Lequeux, Role of dynamical heterogeneities on the viscoelastic spectrum of polymers: A stochastic continuum mechanics model. *Macromolecules* **48**, 6690–6702 (2015).
15. G. A. Parada, X. Zhao, Ideal reversible polymer networks. *Soft Matter* **14**, 5186–5196 (2018).
16. W. C. Yount, D. M. Loveless, S. L. Craig, Small-molecule dynamics and mechanisms underlying the macroscopic mechanical properties of coordinatively cross-linked polymer networks. *J. Am. Chem. Soc.* **127**, 14488–14496 (2005).
17. S. C. Grindy, R. Learsch, D. Mozhdehi, J. Cheng, D. G. Barrett, Z. Guan, P. B. Messersmith, N. Holten-Andersen, Control of hierarchical polymer mechanics with bioinspired metal-coordination dynamics. *Nat. Mater.* **14**, 1210–1216 (2015).
18. A. M. Rosales, K. S. Anseth, The design of reversible hydrogels to capture extracellular matrix dynamics. *Nat. Rev. Mater.* **1**, 15012 (2016).
19. A. N. Semenov, J.-F. Joanny, A. R. Khokhlov, Associating polymers: Equilibrium and linear viscoelasticity. *Macromolecules* **28**, 1066–1075 (1995).
20. E. Michel, J. Appell, F. Molino, J. Kieffer, G. Porte, Unstable flow and nonmonotonic flow curves of transient networks. *J. Rheol.* **45**, 1465–1477 (2001).
21. Q. Li, D. G. Barrett, P. B. Messersmith, N. Holten-Andersen, Controlling hydrogel mechanics via bio-inspired polymer–nanoparticle bond dynamics. *ACS Nano* **10**, 1317–1324 (2016).
22. A. V. Zhukhovitskiy, J. Zhao, M. Zhong, E. G. Keeler, E. A. Alt, P. Teichen, R. G. Griffin, M. J. A. Hore, A. P. Willard, J. A. Johnson, Polymer structure dependent hierarchy in polyMOC gels. *Macromolecules* **49**, 6896–6902 (2016).
23. Q. Wang, J. L. Mynar, M. Yoshida, E. Lee, M. Lee, K. Okuro, K. Kinbara, T. Aida, High-water-content mouldable hydrogels by mixing clay and a dendritic molecular binder. *Nature* **463**, 339–343 (2010).
24. T. Chatterjee, A. I. Nakatani, A. K. Van Dyk, Shear-dependent interactions in hydrophobically modified ethylene oxide eurethane (HEUR) based rheology modifier–latex suspensions: Part 1. Molecular microstructure. *Macromolecules* **47**, 1155–1174 (2014).
25. P. J. Flory, *Principles of Polymer Chemistry* (Cornell Univ. Press, 1953).
26. A. Gomez-Casado, H. H. Dam, M. D. Yilmaz, D. Florea, P. Jonkheijm, J. Huskens, Probing multivalent interactions in a synthetic host– guest complex by dynamic force spectroscopy. *J. Am. Chem. Soc.* **133**, 10849–10857 (2011).
27. E. M. Bertin, J.-P. Bouchaud, Subdiffusion and localization in the one-dimensional trap model. *Phys. Rev. E* **67**, 026128 (2003).
28. P. Sollich, F. Lequeux, P. Hébraud, M. E. Cates, Rheology of soft glassy materials. *Phys. Rev. Lett.* **78**, 2020–2023 (1997).
29. K. Trachenko, A. Zaccone, Slow stretched-exponential and fast compressed-exponential relaxation from local event dynamics. *J. Phys. Condens. Matter* **33**, 315101 (2021).
30. E. Raspaud, D. Lairez, M. Adam, J.-P. Carton, Triblock Copolymers in a selective solvent. 2. Semidilute solutions. *Macromolecules* **29**, 1269–1277 (1996).
31. N. G. Van Kampen, *Stochastic Processes in Physics and Chemistry* (Elsevier, November 1992).
32. C. Texier, Individual energy level distributions for one-dimensional diagonal and off-diagonal disorder. *J. Phys. A Math. Gen.* **33**, 6095–6128 (2000).
33. A. V. Zhukhovitskiy, M. Zhong, E. G. Keeler, V. K. Michaelis, J. E. P. Sun, M. J. A. Hore, D. J. Pochan, R. G. Griffin, A. P. Willard, J. A. Johnson, Highly branched and loop-rich gels via formation of metal–organic cages linked by polymers. *Nat. Chem.* **8**, 33–41 (2016).
34. L. C. Hsiao, R. S. Newman, S. C. Glotzer, M. J. Solomon, Role of isostaticity and load-bearing microstructure in the elasticity of yielded colloidal gels. *Proc. Natl. Acad. Sci. U.S.A.* **109**, 16029–16034 (2012).
35. J. Colombo, E. Del Gado, Self-assembly and cooperative dynamics of a model colloidal gel network. *Soft Matter* **10**, 4003–4015 (2014).
36. Y. Gu, E. A. Alt, H. Wang, X. Li, A. P. Willard, J. A. Johnson, Photoswitching topology in polymer networks with metal–organic cages as crosslinks. *Nature* **560**, 65–69 (2018).
37. D. Li, J. Zhang, K. Landskron, T. Liu, Spontaneous self-assembly of metal-organic cationic nanocages to form monodisperse hollow vesicles in dilute solutions. *J. Am. Chem. Soc.* **130**, 4226–4227 (2008).
38. J. P. Bouchaud, Weak ergodicity breaking and aging in disordered systems. *J. Phys.* **2**, 1705–1713 (1992).
39. A. Rao, B. D. Olsen, Structural and dynamic heterogeneity in associative networks formed by artificially engineered protein polymers. *Soft Matter* **19**, 6314–6328 (2023).
40. Q. Chen, G. J. Tudryn, R. H. Colby, Ionomer dynamics and the sticky Rouse model. *J. Rheol.* **57**, 1441–1462 (2013).
41. J.-M. Choi, A. S. Holehouse, R. V. Pappu, Physical principles underlying the complex biology of intracellular phase transitions. *Annu. Rev. Biophys.* **49**, 107–133 (2020).
42. O. Lieleg, J. Kayser, G. Brambilla, L. Cipelletti, A. R. Bausch, Slow dynamics and internal stress relaxation in bundled cytoskeletal networks. *Nat. Mater.* **10**, 236–242 (2011).
43. A. Tripathi, K. C. Tam, G. H. McKinley, Rheology and dynamics of associative polymers in shear and extension: Theory and experiments. *Macromolecules* **39**, 1981–1999 (2006).
44. B. Qu, C. Zhu, C. Li, X. Zhang, Y. Chen, Coupling hollow Fe3O4–Fe nanoparticles with graphene sheets for high-performance electromagnetic wave absorbing material. *ACS Appl. Mater. Interfaces* **8**, 3730–3735 (2016).
45. N. Holten-Andersen, M. J. Harrington, H. Birkedal, B. P. Lee, P. B. Messersmith, K. Y. C. Lee, J. H. Waite, pH-induced metal-ligand cross-links inspired by mussel yield self-healing polymer networks with near-covalent elastic moduli. *Proc. Natl. Acad. Sci. U.S.A.* **108**, 2651–2655 (2011).
46. J. Song, M. H. Rizvi, B. B. Lynch, J. Ilavsky, D. Mankus, J. B. Tracy, G. H. McKinley, N. Holten-Andersen, Programmable anisotropy and percolation in supramolecular patchy particle gels. *ACS Nano* **14**, 17018–17027 (2020).

Acknowledgments: H.L.R. and M.L. thank T. Divoux for valuable comments on the manuscript. **Funding:** This work was supported by Marie Curie Integration Grant PCIG12-GA-2012-334053; "Investissements d'Avenir" LabEx PALM (ANR-10-LABX-0039-PALM); ANR grants ANR-15-CE13-0004-03, ANR-21-CE11-0004-02, ANR-22-ERCC-0004-01, and ANR-22-CE30-0024-01; as well as ERC Starting Grant 677532 to M.L. M.L.'s group belongs to the CNRS consortium AQV. This work was supported in part by the NSF Center for the Chemistry of Molecularly Optimized Networks (MONET, CHE-2116298). **Author contributions:** H.L.R. and M.L. designed the theoretical model and performed the theoretical analysis. H.L.R. analyzed the data. J.S. synthetized the ion and nanoparticle gels and carried out their rheological characterization under the supervision of N.H.-A. and G.H.M. A.V.Z. and D.L. synthetized the nanocage gels and carried out their rheological characterization under the supervision of J.A.J. The article was written by H.L.R., J.S., and M.L. The other authors read and edited the manuscript. **Competing interests:** The authors declare that they have no competing interests. **Data and materials availability:** All data needed to evaluate the conclusions in the paper are present in the paper and/or the Supplementary Materials.

Submitted 7 November 2023
Accepted 10 April 2024
Published 15 May 2024
10.1126/sciadv.adl5056

Science Advances
AAAS

Supplementary Materials for

Valence can control the nonexponential viscoelastic relaxation of multivalent reversible gels

Hugo Le Roy *et al.*

Corresponding author: Hugo Le Roy, h.leroy@epfl.ch; Martin Lenz, martin.lenz@universite-paris-saclay.fr

Sci. Adv. **10**, eadl5056 (2024)
DOI: 10.1126/sciadv.adl5056

This PDF file includes:

S1. DISTRIBUTION OF SUPERBOND BREAKING TIME AND DERIVATION OF τ_N

Here we show that the survival probability for the detachment of a superbond (illustrated in main text Fig. 2) containing many polymer strands ($N \to \infty$) asymptotically goes to $S(t) = e^{-t/\tau_N}$, where τ_N is given by Eq. (4) of the main text. We first consider a general one-step process and derive the basic recursion equation used throughout the proof in Sec. S1.1. We solve the recursion in Sec. S1.2 and express the generating function of $S(t)$ as a double sum. In Sec. S1.3, we apply the resulting formula to our particular problem and take the continuum limit of the second sum. Finally, we compute both sums in the $N \to \infty$ limit in Sec. S1.4. Our derivation is adapted from the calculation presented in the appendix of Ref.[32]

S1.1. Backward Kolmogorov equation for the generating function of $S(t)$

We consider a one-step process, *i.e.*, a stochastic process consisting of transitions between consecutive discrete states on a line, with transition rates r_n and g_n illustrated in Fig. S1(a). We denote the probability for the particle to be in state k at time t after starting in state n at time 0 by $P(k,t|n)$. We assume an absorbing boundary condition in 0 and a reflecting boundary condition in N, *i.e.*,

$$\forall n \in [1..N] \quad P(0,t|n) = 0, \qquad r_N = 0. \tag{S1}$$

The backward Kolmogorov equation for our process reads [31]

$$\frac{\mathrm{d}P}{\mathrm{d}t}(k,t|n) = g_n[P(k,t|n+1) - P(k,t|n)] - r_n[P(k,t|n) - P(k,t|n-1)]. \tag{S2}$$

We define the survival probability and its generating function (Laplace transform), respectively as

$$S_n(t) = \sum_{k=1}^{N} P(k,t|n), \quad h_n(\alpha) = \int_0^{+\infty} S_n(t) e^{-\alpha t}\,\mathrm{d}t. \tag{S3}$$

Inserting these definitions into Eq. (S2) yields

$$\alpha h_n(\alpha) - 1 = g_n[h_{n+1}(\alpha) - h_n(\alpha)] - r_n[h_n(\alpha) - h_{n-1}(\alpha)], \tag{S4}$$

which we endeavor to solve for $h_n(\alpha)$ in the following.

S1.2. Sum equation for the generating function

We define a rescaled current between sites $n-1$ and n

$$\Delta_n = \begin{cases} r_n \left(\prod_{i=n}^{N-1} \frac{r_{i+1}}{g_i}\right) [h_n - h_{n-1}] & \text{for } n < N \\ r_N[h_N - h_{N-1}] & \text{for } n = N \end{cases}. \tag{S5}$$

This allows us to turn the two-step recursion of Eq. (S4) into one with only one step:

$$\Delta_n = \begin{cases} \Delta_{n+1} + \left(\prod_{i=n}^{N-1} \frac{r_{i+1}}{g_i}\right) [1 - \alpha h_n] & \text{for } n < N \\ 1 - \alpha h_N & \text{for } n = N \end{cases}, \tag{S6}$$

which can easily be summed as

$$\Delta_n = \left[\sum_{j=n}^{N-1} \left(\prod_{i=n}^{N-1} \frac{r_{i+1}}{g_i}\right) (1 - \alpha h_j)\right] + 1 - \alpha h_N. \tag{S7}$$

We now invert Eq. (S5) and use Eq. (S7) to express the finite difference $(h_n - h_{n-1})$. We further use the property that $h_m = h_0 + \sum_{n=1}^{m}(h_n - h_{n-1})$ and recognize that $h_0 = 0$ due to Eq. (S1) to obtain

$$h_m = \sum_{n=1}^{m} \frac{1}{r_N} \left(\prod_{i=n}^{N-1} \frac{g_i}{r_{i+1}}\right) \left\{ \left[\sum_{j=n}^{N-1} \left(\prod_{i=n}^{N-1} \frac{r_{i+1}}{g_i}\right) (1 - \alpha h_j)\right] + 1 - \alpha h_N \right\}. \tag{S8}$$

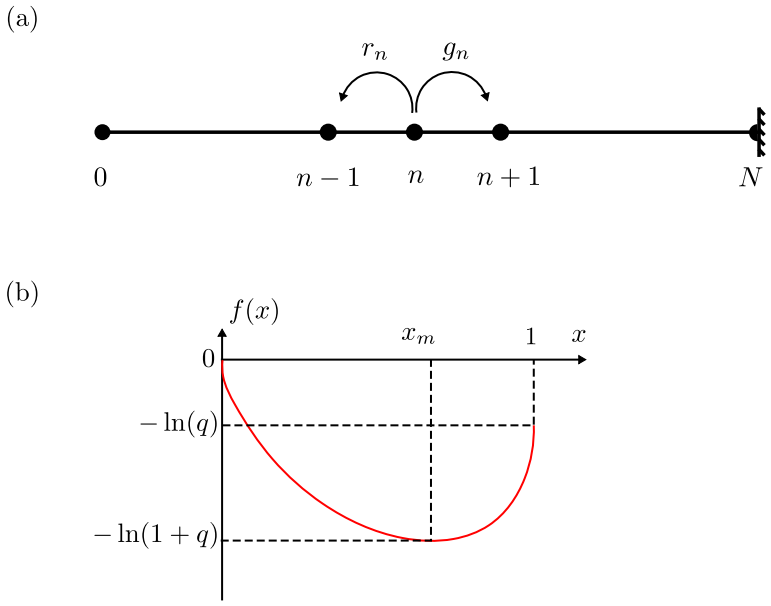

FIG. S1. **Superbond detachment as a Kramers-like barrier-crossing problem.** (a) Definition of the rates of the one-step process. (b) Profile of the pseudo-free energy defined in Eq. (S13). Superbond detachment requires the system to fluctuate out of the free energy well to the $x = 0$ absorbing state, with $1/N$ playing the role of a temperature.

S1.3. Application and continuum limit

Using the mean detachment time of a polymer strand (denoted as ω_- in the main text) as our unit of time and defining $q = \omega_+/\omega_-$, the model of the main text implies

$$\forall n \in [1..N] \quad r_n = n, \quad g_n = (N-n)q, \tag{S9}$$

which we insert into Eq. (S8) to obtain

$$h_n = \sum_{j=1}^{n} \frac{1}{j\binom{N}{j}q^j} \sum_{i=j}^{N} \binom{N}{i} q^i (1 - \alpha h_i). \tag{S10}$$

In Eq. (S10), the outermost sum is dominated by the very small values of j in the limit $N \to \infty$. We thus need only consider small values of j when computing the innermost sum, which happens to be dominated by a value of i far from the edges of the $[1..N]$ interval. We can thus take its continuum limit. Using Stirling's formula, we obtain

$$h_n \underset{N\to\infty}{\sim} \sum_{j=1}^{n} \frac{1}{j\binom{N}{j}q^j} \int_0^1 \sqrt{\frac{N}{2\pi x(1-x)}} e^{-Nf(x)} [1 - \alpha h(x,\alpha)]\, \mathrm{d}x, \tag{S11}$$

where we have defined the continuum version of our generating function though $h(x,\alpha) = h_{Nx}(\alpha)$, as well as the pseudo free energy of the system

$$f(x) = x \ln x + (1-x)\ln(1-x) - x \ln q. \tag{S12}$$

This free energy has a single minimum in $x_m = q/(1+q)$ with a locally parabolic structure given by

$$f(x) = -\ln(1+q) + \frac{(1+q)^2}{2q}(x - x_m)^2 + \mathcal{O}(x - x_m)^3, \tag{S13}$$

which we illustrate in Fig. S1(b). The problem at hand is exactly analogous to a Kramers escape problem from the bottom of this minimum to the $n = 0$ boundary condition, with $N \to \infty$ playing the role of the low-temperature limit.

S1.4. Asymptotic simplifications

Using the Kramers analogy to our advantage, we compute the integral of Eq. (S11) using a saddle-point approximation. We thus find that for any $x \in]0,1[$:

$$h(x,\alpha) \underset{N\to\infty}{\sim} (1+q)^N[1-\alpha h(x_m,\alpha)] \sum_{j=1}^{Nx} \frac{q^{-j}}{j\binom{N}{j}}. \tag{S14}$$

Using Stirling's formula for small values of j reveals that the argument of the sum in Eq. (S14) goes as $(j-1)!\times(Nq)^{-j}$. Therefore, the terms of the sum are simply the terms in an expansion in powers of N. We keep only the lowest-order term to find

$$\forall x \in]0,1[\quad h(x,\alpha) \underset{N\to\infty}{\sim} \tau_N[1-\alpha h(x_m,\alpha)]. \tag{S15}$$

where

$$\tau_N = \frac{(1+q)^N}{Nq} \tag{S16}$$

is the dimensionless version of the mean first-passage time presented in Eq. (4) of the main text.

Setting $x = x_m$, Eq. (S15) implies

$$h(x_m,\alpha) \underset{N\to\infty}{\sim} \frac{1}{\alpha+\tau_N^{-1}} \quad \Leftrightarrow \quad S_{Nx_m}(t) \underset{N\to\infty}{\sim} e^{-t/\tau_N}. \tag{S17}$$

Finally, using Eq. (S15) again yields

$$\forall x \in]0,1[\quad S_{Nx}(t) \underset{N\to\infty}{\sim} -\tau_N \frac{\mathrm{d}S_{Nx_m}}{\mathrm{d}t}(t) = e^{-t/\tau_N}, \tag{S18}$$

which is the exponential distribution presented in the main text.

S2. LINK BETWEEN α AND $N_{\mathrm{sat}}/\bar{N}$

Here establish the connection between the stretch exponent α and the values of $N_{\mathrm{sat}}/\bar{N}$ shown in Fig. 4 of the main text. To mimic the observation of an experimental step strain over a finite time window, we focus our attention on the time interval between $t = 0$ and $t = \tau_{90}$, where τ_{90} is the time required to relax 90% of the stress, *i.e.*, $\sigma(\tau_{90}) = 0.1 \times \sigma(0)$. We plot the relaxation curve given by Eq. (6) of the main text over this time window, then perform a least-squares fit using a stretched exponential [Eq. (1) of the main text] with α and τ as fitting parameters. As shown in Fig. S2, the agreement is excellent for a large majority of the parameters used. The corresponding value of the fitting parameters (τ and α) for a broader variety of $\bar{N}$ and N_{sat} is also provided in Fig. S3. This suggests that experimental curves that are well fitted by a stretched exponential could be equally well described by our model.

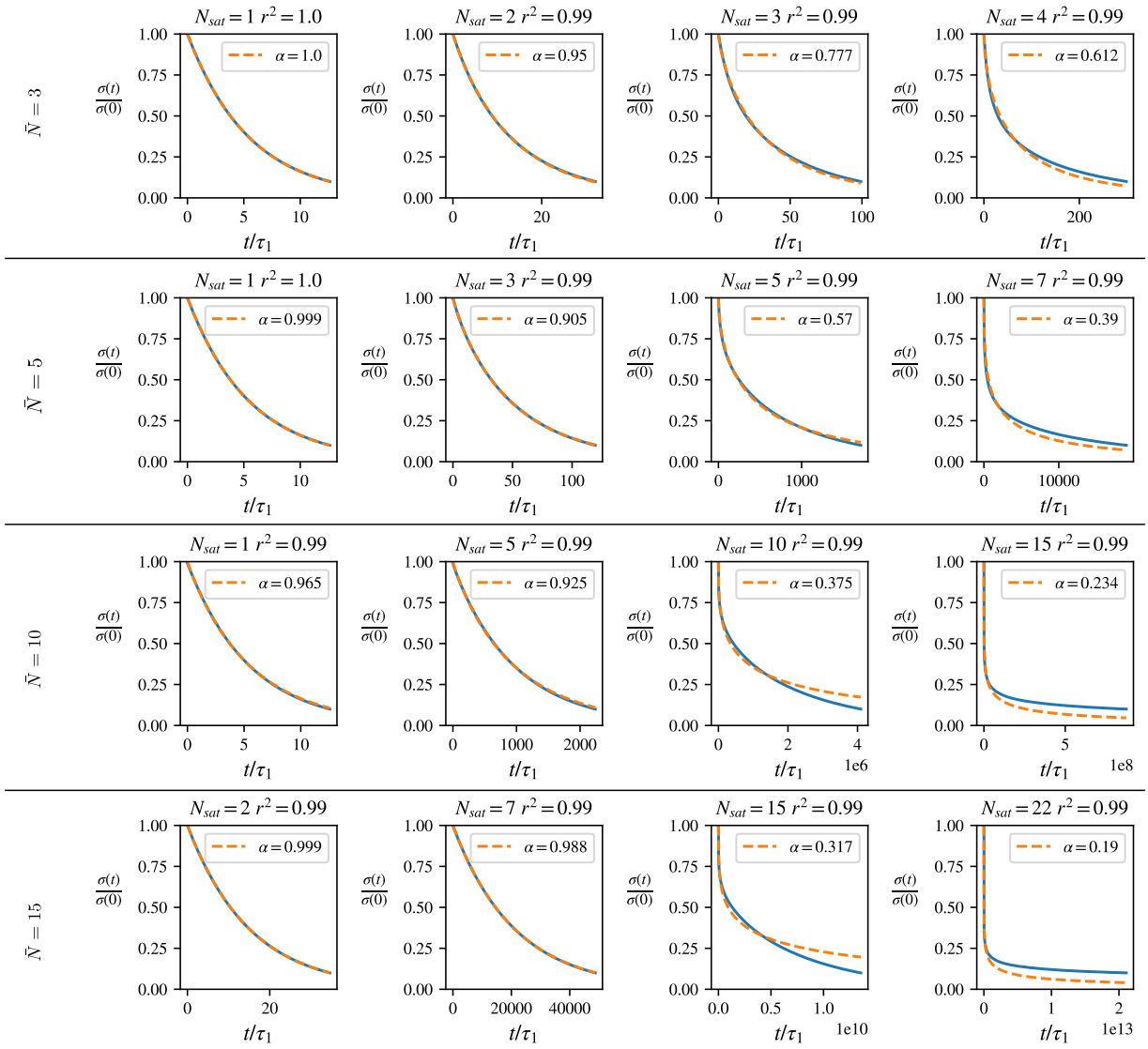

FIG. S2. **Illustration of the similarity of our modeled stress response function with a stretched exponential.** We plot the relaxation modulus computed using Eq. (6) of the main text for $\bar{N} \in [3, 5, 10, 15]$. For each value of $\bar{N}$, we plot four values of $N_{\rm sat}$, namely $N_{\rm sat} = 0.1\bar{N}$, $0.5\bar{N}$, $\bar{N}$ and $1.5\bar{N}$, $p_{\rm off} = 0.2$. Each plot also mentions the value of the fitted stretch exponent α and the correlation coefficient r^2.

S3. TIME-TEMPERATURE COLLAPSE

Here we describe the procedure used to determine the binding energy ΔE in the experimental systems discussed in the main text. Equation (4) of the main text implies that the temperature dependence of the stress response function can be eliminated by expressing it as a function of the rescaled time $\tilde{t} = te^{\beta\Delta E}$. This should cause the relaxation curves of a given system at different temperatures to collapse.

For each type of ligand, we have 5 datasets showing the stress relaxation function as a function of time at each different temperature $\{T^{(\alpha)}\}_{\alpha\in[0,4]} = \{25°\text{C}, 35°\text{C}, 45°\text{C}, 55°\text{C}, 65°\text{C}\}$. To enable the comparison between time-rescaled datasets, we first define an interpolating function for the stress relaxation function at each temperature used. We thus compute the set of interpolating coefficients $\left\{p_k^{(\alpha)}\right\}_k$ by perform a least-square fit of the following rational function

$$P^{(\alpha)}(t) = \sum_{k=-3}^{10} p_k^{(\alpha)} t^k, \tag{S19}$$

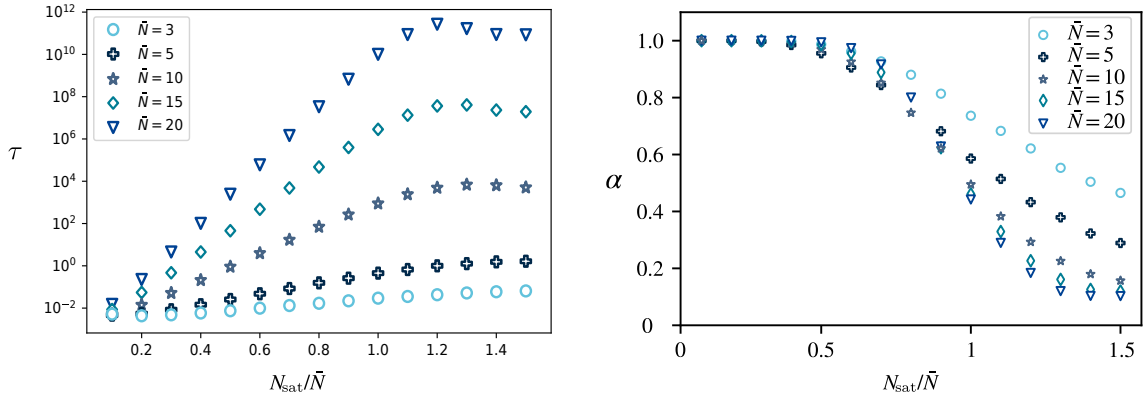

FIG. S3. **Best fit values of the stretched exponential**. We fit the parameters τ and α for a range of values of $\bar{N}$ and $N_{\rm sat}$. The right-hand-side panel is identical to Fig. 4 of the main text.

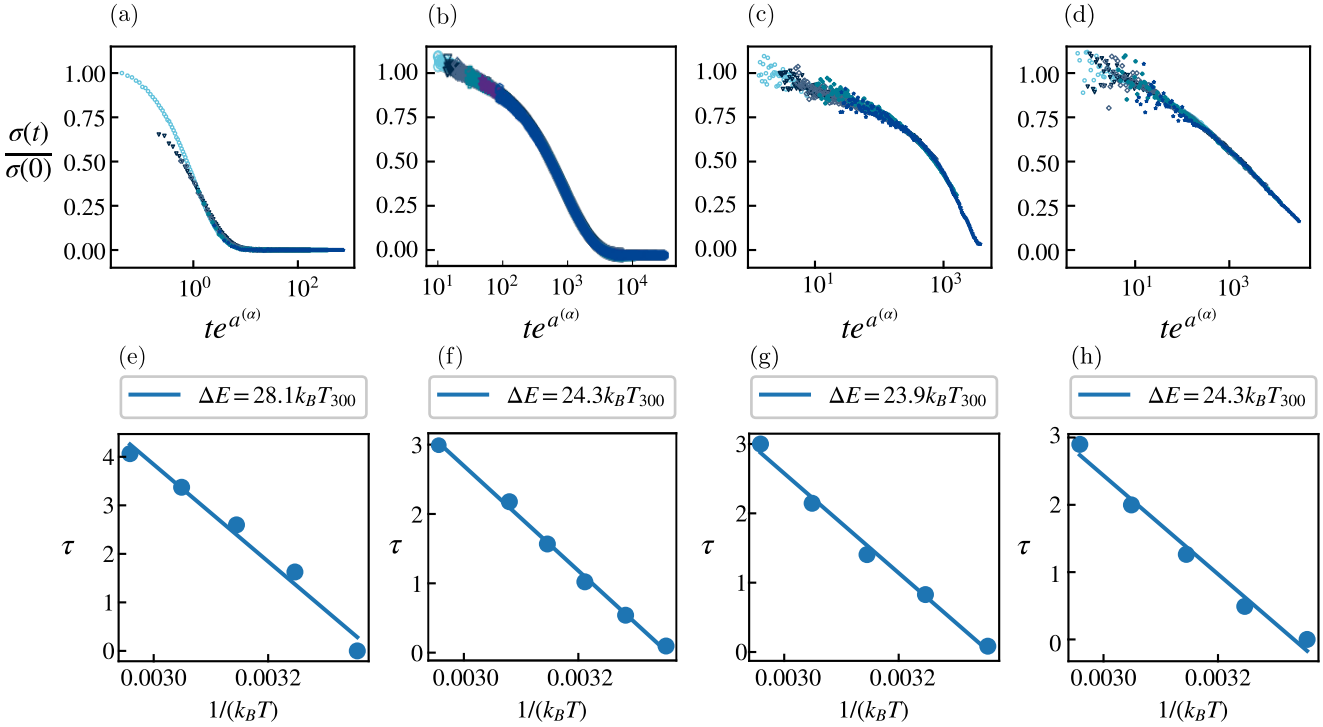

FIG. S4. **Collapse of the relaxation modulus.** (a-c) Collapsed relaxation modulus of Fe^{3+} ions, $Pd_{12}L_{24}$ nanocages and nanoparticles respectively after the rescaling of the time for an optimized collapse . The curves are represented on a log-lin coordinate system, but the collapsing procedure is performed on a lin-lin scale . (d-f) corresponding rescaling parameters as a function of $1/(k_B T)$ the inverse temperature. The slope of the line is $-\Delta E$ and the legend gives the value of ΔE in $k_B T$ unit at $300K$.

to the datapoints $\left\{t_i^{(\alpha)}, \frac{\sigma^{(\alpha)}(t_i)}{\sigma^{(\alpha)}(0)}\right\}_i$. We furthermore define the interval of definition of $P^{(\alpha)}(x)$ as the range over which data is available, *i.e.*, $I_{P^{(\alpha)}} = \left[0, \max_i t_i^{(\alpha)}\right]$.

We then perform the collapse of the $\{T^{(\alpha)}\}_{\alpha\in[1,4]}$ interpolated curves onto the $T^{(0)}$ curve. To this effect we define the set of rescaling coefficients $\{a^{(\alpha)}\}_{\alpha\in[1,4]}$ and performs a separate time rescaling for each temperature: $\tilde{t} = te^{a^{(\alpha)}}$. For each $\alpha \in [1,4]$, we optimise the semidistance

$$D(P,Q) = \int_{I_Q \cap I_P} [P(t) - Q(t)]^2 \mathrm{d}t, \tag{S20}$$

between the functions $t \to P^{(0)}(t)$ and $t \to P^{(\alpha)}(te^{a^{(\alpha)}})$ with respect to $a^{(\alpha)}$. The resulting collapsed curves are shown

in Fig. S4 (a,b,c). The optimal rescaling coefficients are plotted as a function of the inverse temperature $1/k_BT$ in Fig. S4 (d,e,f). Consistent with the time-temperature collapse hypothesis, this dependence is affine, and we use the slope of the best fitting line as our value of the binding energy ΔE.

S4. FIT OF THE STRESS RELAXATION FUNCTION TO OUR THEORETICAL PREDICTION

In the main text, we fit the experimental curves with the stress relaxation function predicted by our model. We then represent them on a log-lin scale to allow the simultaneous visualization of short and long time scales. To demonstrate the robustness of our fits, in Fig. S5 we replot these curves in a lin-lin-scale, as well as a lin-log scale that emphasizes intervals of exponential relaxation as straight lines.

S5. RATIONALIZATION OF THE POISSON DISTRIBUTION OF THE SUPERBOND SIZE $p(N)$

The polymers used in our experiments are 4-arms polyethylene glycol (PEG). At the end of each arm is a nitrocatechol ligand that allows crosslinker binding. In our model, we assume that the ends of a polymer are always attached to a ligand. For this reason, the diffusion of such a polymer over a distance comparable to the polymer size occurs on a time scale comparable to the time required to rearrange the bonds between crosslinkers, which corresponds to the time required for the relaxation of the stress in the system. Let us consider that the 4-arm PEG are able to diffuse over a volume v during the time of the experiment.We model the spreading of the polymers in the system by discretizing the system into small boxes of volume v between which no polymer exchange occurs over the duration of the experiment. As a result the distribution of the polymers over the boxes is due to the initial preparation of the system. We assume that this processes places each polymer in a random box with equal probability. As a result, the probability that a specific box contains n polymers is given by a Poisson distribution:

$$P(n) = e^{-\rho_{\mathrm{PEG}} v} \frac{(\rho_{\mathrm{PEG}} v)^n}{n!}, \tag{S21}$$

where ρ_{PEG} is the average concentration of PEG in the system, and $v\rho_{\mathrm{PEG}}$ is the mean (over the system) number of PEG in a box of volume v. Equation (S21) is the basis for Eq. (5) of the main text.

S6. EXPERIMENTAL FIT USING ALTERNATIVE DISTRIBUTIONS OF N

To demonstrate the robustness of our model, we perform the fit of the experimental data using probability distribution different from the Poisson distribution of Eq. (5) of the main text. For this, we first define three new distributions with the same mean (and when possible the same variance) than the one of Eq. (5) of the main text and keep the saturation value identical to the one in the main text. We first use a rectangular distribution :

$$\text{if } \bar{N} - \sqrt{3\bar{N}} < 0 \quad p_{\mathrm{rectangular}}(N) = \begin{cases} \frac{1}{\bar{N}+\sqrt{3\bar{N}}} & \text{for } N \in [0, \bar{N} + \sqrt{3\bar{N}}] \\ 0 & \text{otherwise} \end{cases} \tag{S22a}$$

$$\text{if } \bar{N} - \sqrt{3\bar{N}} > 0 \quad p_{\mathrm{rectangular}}(N) = \begin{cases} \frac{1}{2\sqrt{3\bar{N}}} & \text{for } N \in [\bar{N} - \sqrt{3\bar{N}}, \bar{N} + \sqrt{3\bar{N}}] \\ 0 & \text{otherwise} \end{cases}, \tag{S22b}$$

a triangular distribution:

$$p_{\mathrm{triangular}}(N) = \begin{cases} \frac{N}{\bar{N}^2} & \text{for } N \in [0, \bar{N}] \\ \frac{2}{\bar{N}} - \frac{N}{\bar{N}^2} & \text{for } N \in [\bar{N}, 2\bar{N}] \\ 0 & \text{otherwise} \end{cases}, \tag{S23}$$

and a linear distribution:

$$p_{\mathrm{linear}}(N) = \begin{cases} \frac{8N}{9\bar{N}^2} & \text{if } N \in [0, 3\bar{N}/2] \\ 0 & \text{otherwise} \end{cases}. \tag{S24}$$

In each of these cases, we introduce a truncation at the maximum superbond size in the same way as in Eqs. (5-6) of the main text (with discrete sums replaced by integrals). The resulting fits are displayed in Fig. S6, and the

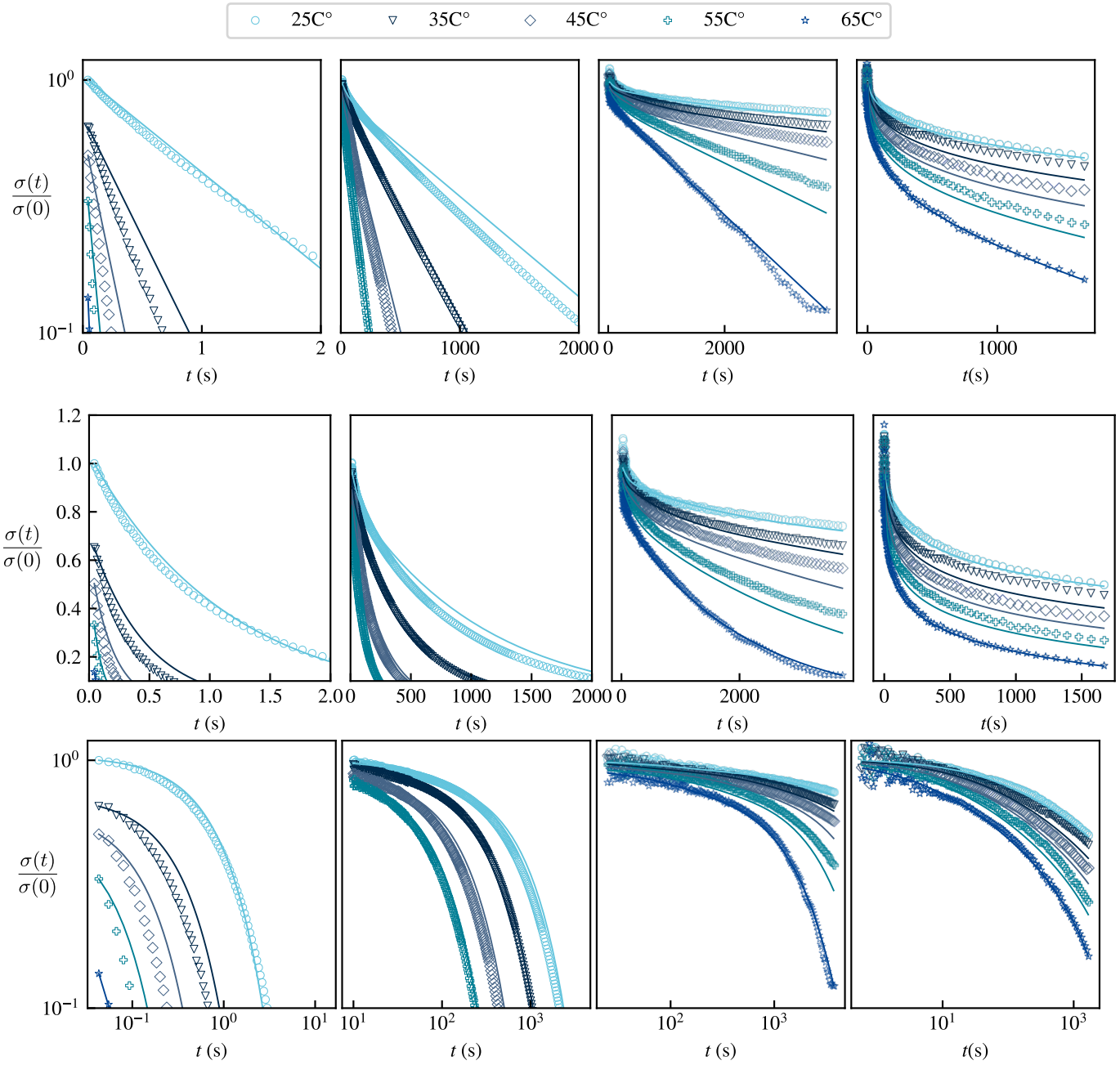

FIG. S5. **Fits of the experimental curves**. Respectively lin-lin and lin-log and log-log representation of Fig. 5 in the main text.

corresponding value of the fitting parameters are given in Table S1. The fitting curves and fitting parameters remain close to the ones obtained in the main text, implying that our specific choice of a Poisson distribution of superbond sizes is not critical for the validity of our results.

S7. DERIVATION OF THE LOG-NORMAL PROBABILITY DISTRIBUTION.

Here we derive Eq. (7) of the main text. Considering the Eq. (5) of the main text without the cutoff due to the valence, the distribution of single strands in a superbond becomes a simple Poisson distribution of mean $\bar{N}$. A random number drawn from such a distribution can also be considered as the sum of $\bar{N}$ independent variables drawn from a

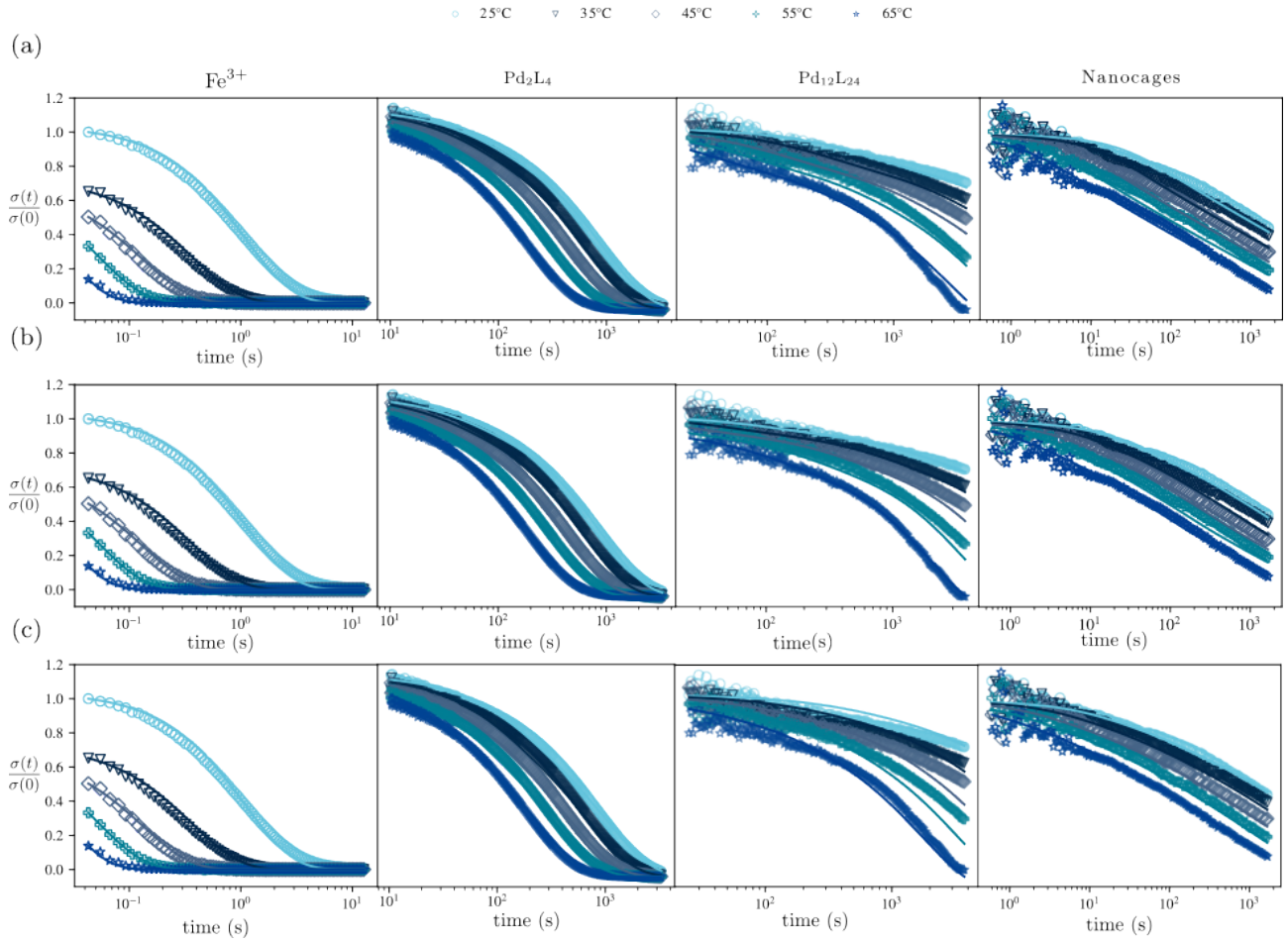

FIG. S6. **Fit of the experimental data using alternative probability distribution of N.** Respectively Fe^{3+}, nanoparticles and nanocage relaxation curves fitted using (a) a uniform distribution, (b) a triangular distribution and (c) using a linear distribution.

	parameter	Fe^{3+}	Pd_2L_4	$Pd_{12}L_{24}$	nanoparticles
uniform	$\mathbf{p_{off}}$	0.08	0.07	0.06	0.3
	τ_1(s)	0.86	122	41	11
	$\bar{\mathbf{N}}$	1	2	4	7
triangular	$\mathbf{p_{off}}$	0.09	0.02	0.03	0.5
	τ_1(s)	0.86	4	83	13
	$\bar{\mathbf{N}}$	1	3	4	5
linear	$\mathbf{p_{off}}$	0.08	0.04	0.07	0.24
	τ_1(s)	0.86	62	$3.9\ 10^2$	5.7
	$\bar{\mathbf{N}}$	1	2	3.3	6.3

TABLE S1. Value of the fitting parameters for the three alternative distributions of N indicated in the left column.

Poisson distribution of mean 1. According to the central limit theorem, the probability distribution of the sum of $\bar{N}$ independent random numbers converges to a normal distribution of mean $\bar{N}$ and variance $\sqrt{\bar{N}}$ for $\bar{N} \gg 1$. Moreover, as the main dependence of τ_N on N is exponential, in the large-$\bar{N}$ limit replacing the factor of N preceding $p_{\rm off}^N$ by the typical value $\bar{N}$ induces only a small (logarithmic) error. We thus approximate: $\tau_N/\tau_1 \sim \exp[N \log(p_{\rm off})]/\bar{N}$, and

write:

$$N = -\frac{\ln(\bar{N}\tau_N/(\tau_1 p_{\text{off}}))}{\ln(p_{\text{off}})}. \tag{S25}$$

Treating N as a continuous variable when computing the stress relaxation function allows us to change variable:

$$\begin{aligned}\frac{G(t)}{G(0)} &= \sum_N p(N)\exp(-t/\tau_N) \\ &\approx \int_N p(N)\exp(-t/\tau_N)dN \\ &= \int_\tau p(\tau)\exp(-t/\tau)d\tau.\end{aligned} \tag{S26}$$

Where we used in the last line the identity:

$$p(\tau)d\tau = p(N)dN, \tag{S27}$$

Substituting N to τ in the approximate normal distribution of N finally gives a log-normal distribution of relaxation time presented in Eq. (7) of the main text.

S8. DERIVATION OF THE POWER LAW RELAXATION

Here we derive Eq. (8) of the main text. As discussed in the main text, substituting the superbond size distribution Eq. (5) of the main text for an exponential distribution

$$p(N) = \left(1 - e^{-1/\bar{N}}\right) e^{-N/\bar{N}} \tag{S28}$$

yields a power-law relaxation regime provided that $\bar{N} \gg 1$, as shown in Fig. S7. Here we compute the value of the relaxation exponent.

Since Eq. (S28) does not saturate at a finite $N = N_{\text{sat}}$, Eq. (6) of the main text becomes

$$\frac{\sigma(t)}{\sigma(0)} = \sum_{N=1}^{+\infty} \frac{p(N)}{1-p(0)} e^{-t/\tau_N} \qquad \text{with} \qquad \tau_N = \frac{\tau_0 e^{\beta\Delta E}}{N p_{\text{off}}^N}. \tag{S29}$$

We employ the same approximation as in Sec. S7, which captures the dominant exponential relationship between τ and N:

$$\tau_N \simeq \frac{\tau_0 e^{\beta\Delta E}}{\bar{N} p_{\text{off}}^N}. \tag{S30}$$

We also take the continuum limit of the sum of Eq. (S29) as is appropriate for large $\bar{N}$. Defining the dimensionless time $\tilde{t} = t\bar{N}/\tau_0 e^{\beta\Delta E}$, this yields

$$\frac{\sigma(t)}{\sigma(0)} \underset{\bar{N}\gg 1}{\sim} \int_0^{+\infty} p(N) e^{-\tilde{t} p_{\text{off}}^N}\, \mathrm{d}N. \tag{S31}$$

We next change our integration variable to $\tilde{\tau} = p_{\text{off}}^N$ to find

$$\frac{\sigma(t)}{\sigma(0)} \underset{\bar{N}\gg 1}{\sim} \int_1^{+\infty} \gamma \tilde{\tau}^{-(1+\gamma)} e^{-\tilde{t}/\tilde{\tau}}\, \mathrm{d}\tilde{\tau} \underset{\bar{N}\gg 1, \tilde{t}\gg 1}{\sim} \Gamma(1+\gamma)\tilde{t}^{-\gamma}, \qquad \text{where} \qquad \gamma = -\frac{1}{\bar{N}\ln p_{\text{off}}} > 0 \tag{S32}$$

and where Γ denotes the gamma function. Equation (S32) implies the power law presented in Eq. (8) of the main text, and its accuracy at long times is confirmed by the plots of Fig. (S7). As discussed in the main text in relation to trap models, here an exponential distribution of N combined with an exponential dependence of the relaxation time on N [Eq. (S29)] result in a power law distribution of the relaxation times. This distribution is apparent in the integral on the left of Eq. (S32), and eventually results in the power law relaxation. Note that the approximation of Eq. (S30) leads us to ignore a possible logarithmic dependence of $\sigma(t) \times t^\gamma$ on t, hence the small mismatch between the curves of Fig. S7.

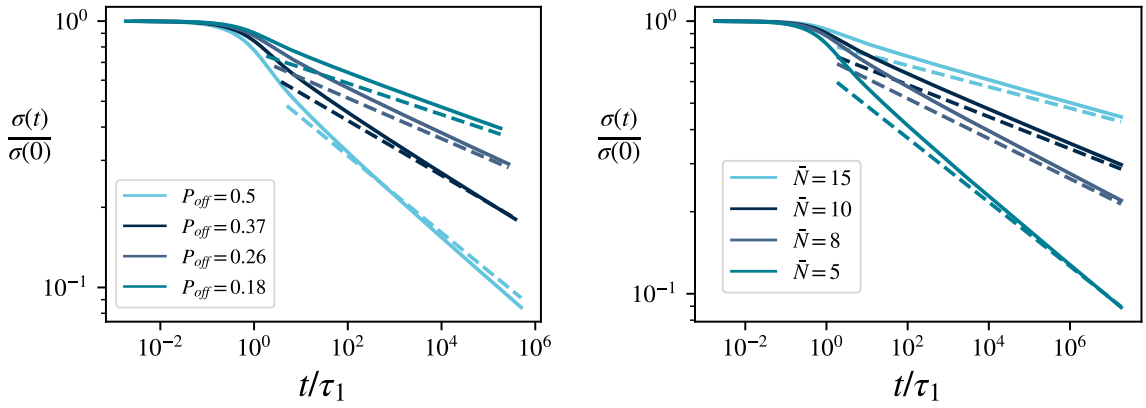

FIG. S7. **Comparison between exact and approximate expression of relaxation modulus**. The exact expression is given in Eq. (S29) (solid lines) and the approximate expression in Eq. (S32) (dashed lines).

S9. SCALING REGIMES FOR THE COMPLEX MODULUS

Here we derive Eq. (9) of the main text, the associated prefactors and its extension to $\gamma \geqslant 1$. In the linear response regime, the Fourier transform of the stress is related to that of the strain ϵ through the material's complex modulus G:

$$\sigma(\omega) = G(\omega)\epsilon(\omega). \tag{S33}$$

Denoting the Heaviside step function by H, we consider the response to a step strain $\epsilon(t) = \epsilon_0 H(t)$ and thus obtain $\sigma(\omega)$ by Fourier transforming Eq. (S29). Equation (S33) then yields

$$\int_0^{+\infty} e^{-i\omega t}\sigma(0) \sum_{N=1}^{N_{\rm sat}} \frac{p(N)}{1-p(0)} e^{-t/\tau_N}\,\mathrm{d}t = G(\omega)\int_{-\infty}^{+\infty} e^{-i\omega t}\epsilon_0 H(t)\,\mathrm{d}t \tag{S34}$$

where the bounds of the left-hand-side integral stem from the implicit assumption that $\sigma(t<0)=0$ in Eq. (S29). We compute both integrals in Eq. (S34) to find

$$\tilde{G}(\omega) = \sum_{N=1}^{N_{\rm sat}} \frac{p(N)}{1-p(0)} \frac{i\omega\tau_N}{1+i\omega\tau_N}, \tag{S35}$$

where $\tilde{G}$ is the dimensionless modulus obtained by normalizing G by the high-frequency elastic plateau $\sigma(0)/\epsilon_0$.

In the following we consider a generalization of Eq. (S28) where $p(N) \propto \exp(-N/\bar{N})$ for $N \leq N_{\rm sat}$ and $p(N) = 0$ for $N > N_{\rm sat}$. We analyze the scaling behavior of the storage modulus $G'(\omega) = \Re[G(\omega)]$ and the loss modulus $G''(\omega) = \Im[G(\omega)]$ computed from Eq. (S35).

In the high-frequency regime $\omega \gg \tau_1^{-1}$, the system displays a Maxwell-like rheology:

$$\tilde{G}'(\omega) \underset{\tau_1^{-1}\ll\omega}{\sim} 1 \tag{S36a}$$

$$\tilde{G}''(\omega) \underset{\tau_1^{-1}\ll\omega}{\sim} \frac{e^{-1/\gamma\bar{N}}(1-e^{-1/\bar{N}})}{[1-e^{-(1+\gamma^{-1})/\bar{N}}]^2}\frac{1}{\omega\tau_1}. \tag{S36b}$$

We now consider the intermediate frequency regime $\tau_{N_{\rm sat}}^{-1} \ll \omega \ll \tau_1^{-1}$ in the case $N_{\rm sat} \gg 1$. Provided we also assume $1 \ll \bar{N} \ll N_{\rm sat}$, the approximate power law response of Eq. (S32) applies and we obtain

$$\tilde{G}'(\omega) \underset{\tau_{N_{\rm sat}}^{-1}\ll\omega\ll\tau_1^{-1}}{\sim} \begin{cases} \frac{\pi\gamma/2}{\sin(\pi\gamma/2)} e^{-1/\bar{N}} \left(\frac{\omega\tau_1}{\bar{N}}\right)^{\gamma} & \text{if } \gamma < 2 \\ \frac{\gamma}{\gamma-2} e^{-2/\gamma\bar{N}} \left(\frac{\omega\tau_1}{\bar{N}}\right)^{2} & \text{if } \gamma > 2 \end{cases} \tag{S37a}$$

$$\tilde{G}''(\omega) \underset{\tau_{N_{\rm sat}}^{-1}\ll\omega\ll\tau_1^{-1}}{\sim} \begin{cases} \frac{\pi\gamma/2}{\cos(\pi\gamma/2)} e^{-1/\bar{N}} \left(\frac{\omega\tau_1}{\bar{N}}\right)^{\gamma} & \text{if } \gamma < 1 \\ \frac{\gamma}{\gamma-1} e^{-1/\gamma\bar{N}} \left(\frac{\omega\tau_1}{\bar{N}}\right) & \text{if } \gamma > 1 \end{cases}. \tag{S37b}$$

Finally, at low frequencies $\omega \ll \tau_{N_{\rm sat}}^{-1}$, the system again goes to a Maxwell-like rheology:

$$\tilde{G}'(\omega) \underset{\omega \ll \tau_{N_{\rm sat}}^{-1}}{\sim} A(\gamma, \bar{N})(\omega\tau_1)^2 \tag{S38a}$$

$$\tilde{G}''(\omega) \underset{\omega \ll \tau_{N_{\rm sat}}^{-1}}{\sim} B(\gamma, \bar{N})(\omega\tau_1), \tag{S38b}$$

where the functions A and B take simple forms in the $N_{\rm sat} \gg \bar{N}$ limit:

$$A(\gamma, \bar{N}) = \begin{cases} (1 - e^{1/\bar{N}}) \exp\left[-\frac{N_{\rm sat}(\gamma-2)+\gamma+2}{\gamma \bar{N}}\right] \Phi(e^{(2/\gamma-1)/\bar{N}}, 2, -N_{\rm sat}) & \text{if } \gamma < 2 \\ \left(1 - e^{-1/\bar{N}}\right) e^{(1-2/\gamma)/\bar{N}} \mathrm{Li}_2\left[e^{(2/\gamma-1)/\bar{N}}\right] & \text{if } \gamma > 2 \end{cases} \tag{S39a}$$

$$B(\gamma, \bar{N}) = \begin{cases} \frac{1-e^{-1/\bar{N}}}{N_{\rm sat}} \frac{\exp\left[(1/\gamma-1)N_{\rm sat}/\bar{N}\right]}{\exp\left[(1/\gamma-1)/\bar{N}\right]-1} & \text{if } \gamma < 1 \\ \left(1 - e^{-1/\bar{N}}\right) e^{(1-1/\gamma)/\bar{N}} \ln\left[\frac{1}{1-\exp\left[(1/\gamma-1)/\bar{N}\right]}\right] & \text{if } \gamma > 1 \end{cases}. \tag{S39b}$$

Here Φ denotes the Lerch zeta function defined as $\Phi(z, s, \alpha) = \sum_{n=0}^{\infty} z^n/(n+\alpha)^s$, which simplifies for $z \ll 1$ and $\alpha \gg 1$ (i.e. $p_{\rm off} \ll e^{-2}$ and $N_{\rm sat} \gg 1$) into $\Phi(z, s, \alpha) \sim \alpha^{-s}/(1-z)$. Li_2 denotes the polylogarithm function of order 2, which is defined as $\mathrm{Li}_2(x) = \sum_{k=1}^{\infty} x^k/k^2$. The three successive regimes described by Eqs. (S36-S38) are shown in Fig. S8.

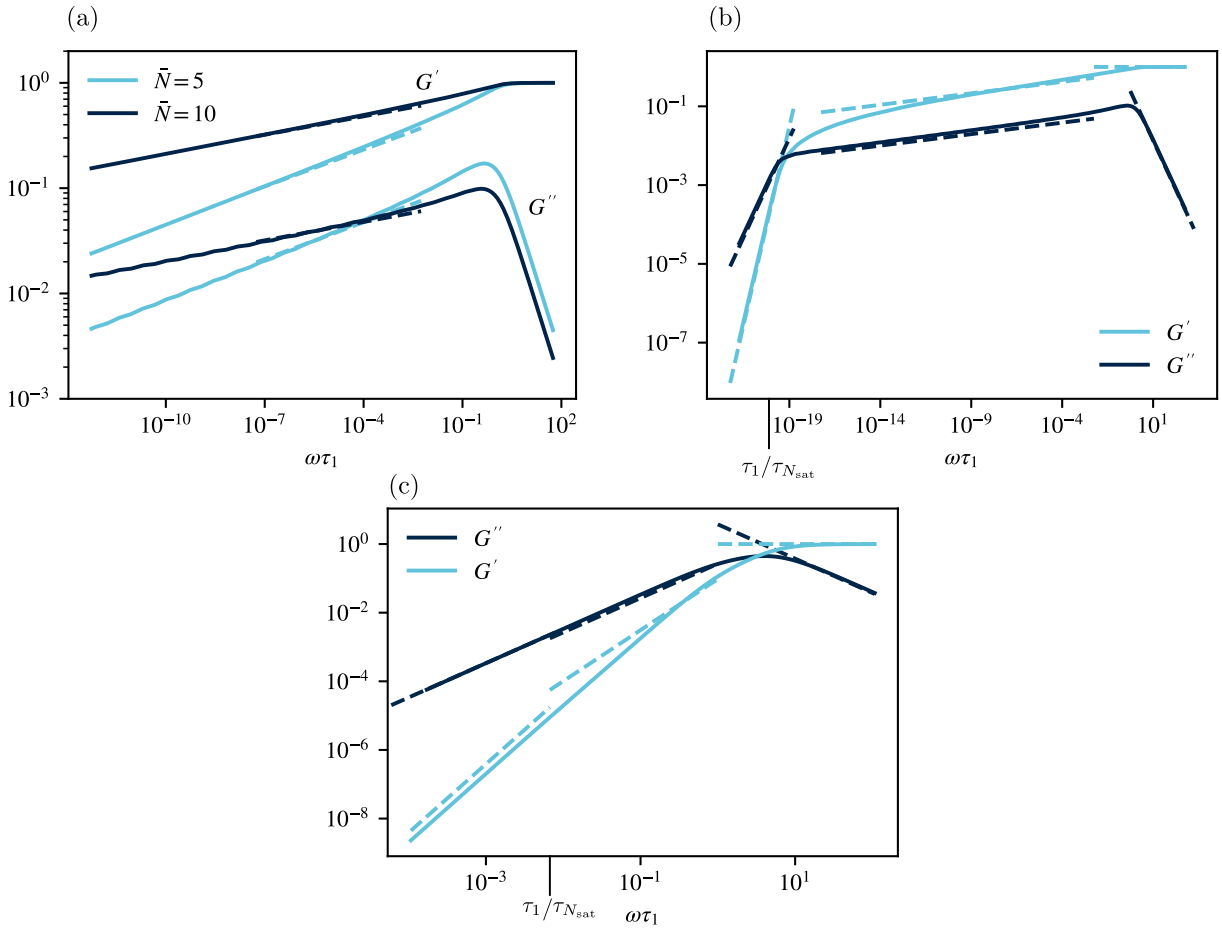

FIG. S8. Comparison between the storage and loss moduli computed from the exact expression Eq. (S35) (solid lines) and the asymptotic expressions of Eqs. (S36-S38) (dashed lines). (a) Plots in the large $N_{\rm sat}$ limit (here $N_{\rm sat} = 100$), showing a good agreement with the power law regime of Eq. (S37) for two values of $\bar{N}$ and for constant $p_{\rm off} = 0.18$ corresponding to $\gamma \simeq 0.116$ and $\gamma \simeq 0.0583$. (b) Plots for a smaller value of $N_{\rm sat}$ ($N_{\rm sat} = 30$) showing the three distinct asymptotic regimes. Here $\bar{N} = 10$ and $p_{\rm off} = 0.18 \Rightarrow \gamma \simeq 0.0583$. (c) Plot of the three distinct asymptotic regimes for a higher value of γ ($\bar{N} = 10$ and $p_{\rm off} = 0.935 \Rightarrow \gamma = 1.49$). The marker at $\omega\tau_1 = \tau_1/\tau_{N_{\rm sat}}$ denotes the expected position of the low-frequency crossover, while the high-frequency crossover is expected for $\omega\tau_1 \approx 1$.